The design and experimental characterisation of a stigmatic XUV instrument for laser plasma spectroscopy.

A thesis submitted for the degree of

Master of Science

by

R. B. Hopkins, B.Sc..

School of Physical Sciences,
Dublin City University.

April 1992.

Research supervised by

J. - P. Mosnier, Ph.D..

This thesis is based on the work of the author

It is dedicated to Kelma, Bobby, Danny and Karen,
without whose support, it would not have been possible

In its origin, science is inseparable from
the collecting and ordering of experiences,
gained in the struggle for existence,
which enabled our ancestors
to raise mankind to its present position
among the other living things that inhabit our earth

Niels Bohr

We have asked so many fundamental questions
which science has gone some way toward answering
Our depth of understanding of the universe is astounding,
yet we as a species preoccupy ourselves with the conversion
of knowledge into technology, able to find neither time nor reason
to look around us with awe

Bruce Hopkins

Contents

Abstract

The optical system of an extreme ultra-violet (XUV) spectrograph was modified to produce high speed, spatially resolved spectra of small sources in the spectral range of about 5 to 25 nm This was achieved by the use of a toroidal focusing mirror placed before the spectrograph The instrument was used to record photoabsorption spectra of laser-produced plasmas in a technique employing a continuum emitted by a second laser plasma, known as the dual laser-produced plasma (DLP) method

The optical theory of the spectrograph and the toroidal mirror are examined in chapter 1 to analyse the imaging properties of the system and determine how best to use a toroidal mirror to compensate for the main aberrations of the concave grating The spectrograph and experimental arrangement, as previously used to achieve DLP photoabsorption, is described in detail in chapter 2 This description includes a characterisation of the optical system by ray-tracing The modifications to the experiment required to effect the improvements are described in chapter 3 This includes a description of the design of the optical system, housing and mounting structures and vacuum system The alignment process and experimental method are detailed in the form of an user's guide and the chapter is concluded by an in-depth analysis of the imaging properties of the spectrograph system by ray-tracing

The final chapter contains a presentation of the experimental results obtained after careful testing and optimisation of the instrument. The combination of time and space resolution has facilitated the isolation of singly ionised aluminium, the photoabsorption spectrum of which is presented here for the first time The experimental results are compared to the ray-tracing analyses to test the validity of the modelling process and the spatial characteristics of the photoabsorption experiment are thus deduced The salient features of the optical system before and after modification are compared to determine the performance gain achieved The thesis is concluded by a critical appraisal of the instrument as a tool for studying the photoabsorption spectroscopy of laser plasmas.

Introduction

Atomic and molecular spectroscopy has provided basic information leading to the development of quantum mechanics and to an understanding of the structure of matter. New data continue to provide insight into atomic structure. Fundamental quantities, such as wavelength and transition probabilities, determined using spectroscopy are of direct importance to many areas of research such as astrophysics (*e g* determination of relative cosmic abundances of elements) and laser physics (*e g* x-ray laser schemes)

The techniques and theory of optical spectroscopy have been thoroughly investigated, current research concentrating on the higher energy regime of inner shell processes, observed through studies of hot, ionised matter The corresponding region of the electromagnetic spectrum is from about 1 to 100 nm (the soft x-ray and extreme ultra-violet or XUV region).

Relatively little is known about inner shell processes due to both the experimental difficulties encountered in producing and analysing ionised matter in the laboratory and the theoretical complexity involved in describing such systems

The experimental difficulties are compounded by the fact that the cross-sections for inner shell excitation or ionisation are usually small and the inner shell vacancies thus produced are predominantly autoionising, that is, non-radiative decay probabilities are much higher than radiative decay probabilities The resultant transitions are not, therefore, generally observed in emission, but only in photoabsorption experiments

The implementation of an XUV photoabsorption experiment requires the generation of a sufficiently high density of excited atoms or ions through which is passed an intense, spectrally smooth XUV continuum beam. Progress in XUV photoabsorption has been hampered for many years by the lack of small, low cost ion and XUV continuum sources Various techniques were developed during the 1960's and 70's, most featuring ion production by furnace or heat-pipe and continuum emission by synchotron or spark source Such systems are both expensive and cumbersome

Initially applied to emission spectroscopy, the laser-produced plasma has proven to be a versatile source of both highly ionised atoms and continuum radiation. Laser plasmas are easy to produce and reproduce, insensitive to ambient pressure variations and of small, almost point-like, spatial extent To date, many comprehensive articles[1] have reviewed the generation, characteristics and applications of laser produced plasmas, so this discussion will briefly deal with the topics relevant to this work

A laser-produced plasma is generated by focusing the output of a high-power (typically Q-switch pulsed) laser on a solid target Such a plasma is short-lived lasting about as long as

[1] See general reference list at the end of the section

the optical pulse The high power density at the focus (of the order of 10^{16} Wm ^{2}) produces a hot, dense plasma with average electron temperature of the order of 10 eV and electron density of the order of 10^{19} cm ^{3} (electron and ion densities are usually comparable) The widely varying and, to some extent, controllable conditions observed in laser plasmas have made them a versatile and rapidly developing area of basic and applied research

Although short-lived, laser-produced plasmas emit an intense burst of radiation over a broad spectral region making them ideally suited to spectroscopic studies Their spectra generally consist of lines (due to bound transitions in atoms and ions) and continuum (due to either Bremsstrahlung or recombination radiation or both) Utilising the fact that the relative contributions from Bremsstrahlung, recombination and discrete emission depend mainly on the target material, laser-produced plasmas of certain elements were found to emit virtually line-free continua in the XUV This lead to the development of the dual laser plasma (DLP) photoabsorption technique [1], a tabletop system requiring only (one or more) high-power lasers and targets composed of suitable (spectrally pure) elements

Many technical difficulties are encountered in the implementation of experiments to analyse XUV radiation Air, particularly oxygen, is opaque to XUV radiation so experiments are carried out under vacuum In fact, no known materials are transparent to such short wavelengths, necessitating the use of reflective optics rather than conventional transmissive optics Furthermore, at XUV wavelengths, refractive index is complex, the imaginary part being a measure of absorption in the medium and the real part characterising reflective and refractive properties The real part is slightly less than unity, producing total external reflection, but so close to unity that reflectivity rises to a useful level only at very large angles of incidence (grazing incidence) So to produce an XUV spectrum requires a reflection-based dispersing element which can be operated at grazing incidence. This is the major constraint facing spectroscopists in the short wavelength range

The concave diffraction grating has two outstanding properties. it has the ability to disperse and focus radiation by reflection and it can be operated at grazing incidence Thus, use of a concave grating in grazing incidence mode allows the entire XUV region to be investigated. The imaging properties of the concave grating are described in detail in chapter one Suffice it to say that commercially available spectrographs with a narrow (adjustable) entrance slit mounted at the source position and a detector mounted along the imaging plane of the grating are the basis for current laser-produced plasma XUV spectroscopy

Having established the basic experimental principle, an historical perspective on the development of the DLP technique will now be presented.

The first DLP experiment to employ a continuum probe followed a comprehensive survey of the spectra emitted by various metals by Carroll *et al* [2] Having developed the continuum source, P K Carroll and E T Kennedy [1] applied it to producing the absorption spectrum of singly ionised lithium (Li^{+}) Both the tungsten probing plasma and the lithium absorbing plasma were generated using a Q-switched ruby laser. The spectra were recorded on

photographic plates using a grazing incidence spectrograph

The DLP technique was adopted by G Tondello *et al* [3] in 1984 This group had been working on improving the efficiency and imaging characteristics of grazing incidence instruments for laser plasma spectroscopy for some years [4, 5] (indeed it is principally their work that this project is based on) Early work by W A Rense and T Violett [6] introduced a grazing incidence toroidal mirror to focus the sun's radiation on the entrance of a vacuum ultra-violet spectrograph to improve the image quality of spectra photographed from space Tondello *et al* modified this technique for application to small sources rather than distant ones for use with laser-produced plasmas

In 1986, Carroll and Costello [7] extended the capability of the DLP technique by using two temporally synchronised lasers This system had the advantage of increased power density on the target and variable inter-plasma time delay (from 250 ns up to 100 μs)

The work described in this thesis involved introducing toroidal optics to an XUV spectrograph as part of a collaborative effort lead by E T Kennedy to build a multilaser DLP system Two synchronised lasers generate the plasmas with a time delay in the range of 0 to 100 μs, and a third, tunable laser, facilitates pumping of selected energy levels in the absorbing plasma The resultant radiation beam may be produced and analysed in either of two systems One records the spectra photoelectrically for computerised display and analysis, the other records spectra photographically Both systems use toroidal mirrors to couple the beam onto their gratings, the photographic system further utilises the focusing properties of the mirror to produce spatially resolved spectra over a limited spectral region

The following dissertation describes in detail the reasons for and the nature of improvements made to the photographic system by introducing toroidal optics Chapter one will outline the theory of the concave grating, showing how operation at grazing incidence produces aberrations in the spectra, and the theory of the toroidal mirror, showing how it can compensate for the main imperfections of the grating. Chapters two and three will describe the experimental apparatus before and after modification, including a description of the optical modelling procedures used to characterise the system The remainder of the thesis presents the experimental results and a critical appraisal of the system.

References

1 Carroll, P K., Kennedy, E T, Phys Rev Lett , 38, 1068 (1977)

2. Carroll, P K , Kennedy, E T and O'Sullivan, G , Opt Lett , 2, 72 (1978)

3 Jannitti, E , Nicolosi, P and Tondello, G , Physica , 124C, 139 (1984)

4 Tondello, G , Optica Acta, 26, 357 (1979)

5 Tondello, G , Jannitti, E , Nicolosi, P and Santi, D , Opt Comm , 32, 281 (1980)

6. Rense, W A and Violett, T, J Opt Soc Am , 49, 139 (1959)

7. Carroll, P. K. and Costello, J T, Phys Rev. Lett., 57, 1581 (1986)

General references

Brilly, J , M Sc thesis, Dublin City University (1986) (unpublished)

Brilly, J , Ph D thesis, Dublin City University (1990) (unpublished)

Carroll, P K and Kennedy, E T , *"Laser-Produced Plasmas"*, Cont Phys , 22, 61 (1981)

Carroll, P K , Kennedy, E T and O'Sullivan, G , *"Table-Top EUV Continuum Light Source"*, IEEE J Quant Elec , QE-19, 1807 (1983)

Costello, J T , Ph D thesis, University College Dublin (1986) (unpublished)

Costello, J T , Mosnier, J-P, Kennedy, E T , Carroll, P K and O'Sullivan, G , *"XUV Absorption Spectroscopy with Laser-Produced Plasmas, A Review"*, Physica Scripta, T34, 77 (1991) (Proceedings of 22nd EGAS Conference)

Kennedy, E T , Ph D thesis, University College Dublin (1977) (unpublished)

Kennedy, E T , Costello, J T and Mosnier, J - P , *"Applications of Laser Plasmas in XUV Photoabsorption Spectroscopy"*, (1991) (Proceedings of the 1991 SPIE Conference)

Key, M H , *"XUV and X-Ray Spectroscopy of Laser-Produced Plasmas"*, Edinburgh University Press, (1988) (lecture published in the Proceedings of the 33rd Scottish Universities Summer School *"Astrophysical & Laboratory Spectroscopy"*).

Svanberg, S , *"Atomic and Molecular Spectroscopy"*, Springer-Verlag (1991).

Chapter 1

Theory

In this chapter, the geometric optical theory of the concave grating is developed to analyse the imaging properties of the grazing incidence spectrograph The geometry is then modified so that a similar treatment can be applied to the toroidal mirror Some of the mathematical detail required for a complete derivation of the equations will be omitted as it is beyond the scope of this discussion

1.1 The concave diffraction grating

Originally developed by H A Rowland [1], in 1882, the concave grating has the following focusing properties If the grating (of radius of curvature R) is positioned at a tangent to a circle of radius 0 5R (with the grating centre on the circumference), the spectrum of an illuminated point on the circle (the source point) is focused on the circle (see figure 1.1) This is known as the Rowland circle mount

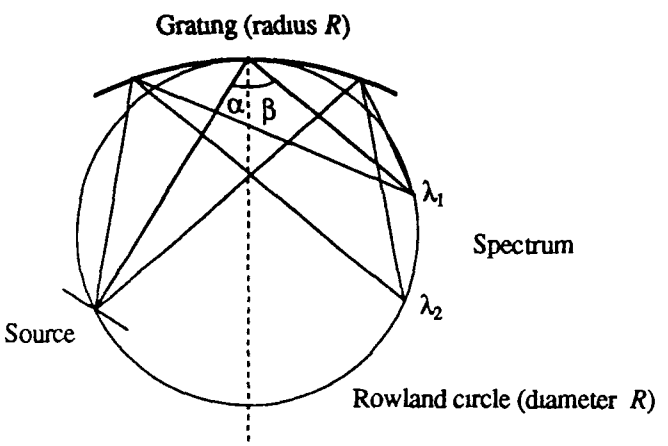

Figure 1.1. The Rowland Circle mount Radiation from the source is dispersed and focused by the grating at λ_1, λ_2 etc α and β are the angles of incidence and diffraction, respectively (after Samson [2])

The most complete geometrical treatments of concave grating theory have been developed by H. G. Beutler [3] and T. Namioka [4], Namioka's work being necessitated by the fact that Beutler's untimely death left his work unfinished.

1.1.1 General theory

The origin, O, of the Cartesian coordinate system is taken to be the grating centre. The x axis is the grating normal with the z axis parallel to the rulings. Let $A(x, y, z)$, $B(x',y',z')$ and $P(u, w, l)$ be points on the source, image and grating respectively (see figure 1.2).

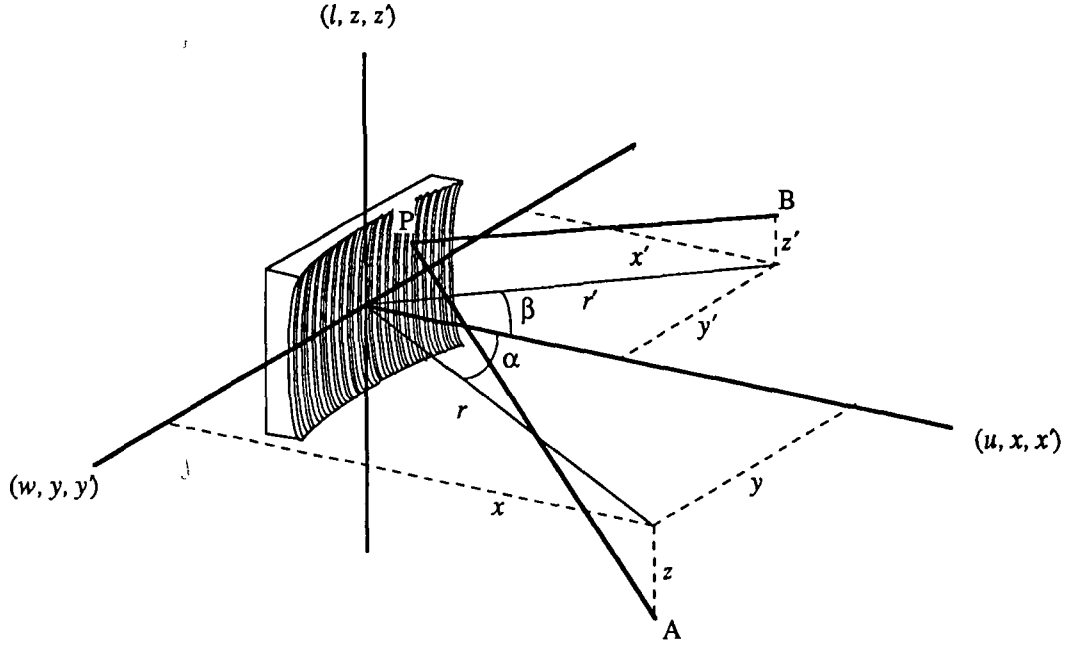

Figure 1.2. Coordinate system for analysis of image formation by the concave diffraction grating

The condition for rays reflected from adjacent rulings to reinforce at B is that the path difference be an integral number of wavelengths This integer, m, is the spectral order. The path difference for any two grooves separated by w is $m\lambda w/d$, where d is the distance between adjacent grooves and λ is the wavelength If a ray from the point A is to be focused at B, contributing to the image, its path APB, where P can be any point on the grating surface, must satisfy the optical path function, F, given by

$$F = AP + BP + m\lambda w/d \qquad (1.1a)$$

To get a focus from a section of the grating, we invoke Fermat's Principle of Least Time which states that the optical path length is stationary across the grating surface, that is, allowed values of w and l are those which cause F to be at an extremum (*i.e* a maximum, minimum or point of inflexion) Thus, for any horizontal section, the condition is that the partial derivative of F with respect to w be zero,

$$\frac{\partial F}{\partial w} = 0, \qquad (1.2a)$$

similarly a focus from a vertical section requires that

$$\frac{\partial F}{\partial l} = 0 \qquad (1\ 2b)$$

The geometrical explanation for these conditions is as follows Equations (1.2a) and (1 2b) have the geometrical significance of angles. If their values are zero then light from A, reflected at P, is directed toward B Non-zero values of the partial differentials indicate that the light is not directed toward B and the image formation is not perfect (see figure 1 3)

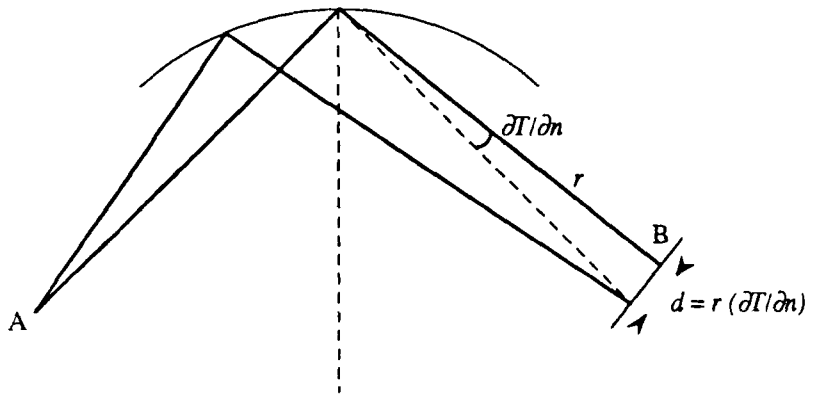

Figure 1.3. The geometry of Fermat's principle

The light must also arrive at B with the same phase in order to produce reinforcement. This phase condition must be fulfilled (over the grating surface) to within a quarter wavelength (according to Rayleigh's quarter wavelength rule[2]) Thus the integral of the path difference, over the width and length of the grating respectively, must not exceed $\pm \lambda/4$, that is

$$\Delta F_w = \int_w \frac{\partial F}{\partial w}\, dw \le \frac{\lambda}{4}, \qquad (1\ 3a)$$

and

$$\Delta F_l = \int_l \frac{\partial F}{\partial l}\, dl \le \frac{\lambda}{4}. \qquad (1\ 3b)$$

Thus equation (1 1a) may be written more precisely as

$$F = AP + BP + m\lambda w/d \pm \lambda/4 \qquad (1.1b)$$

For further analysis, the optical path function must be evaluated as follows. The lengths of AP and BP (in Cartesian coordinates) can be expressed as

$$|AP|^2 = (x - u)^2 + (y - w)^2 + (z - l)^2, \qquad (1.4a)$$

[2] It was first shown by Rayleigh [5] that, in the presence of commonly occurring aberrations, the quality of an image is not seriously affected when the wavefront deformation is less than a quarter of a wavelength.

$$|BP|^2 = (x' - u)^2 + (y' - w)^2 + (z' - l)^2. \qquad (1.4b)$$

As these expressions are identical in form (except for the primed coordinates in (1.4b)), only the derivation of AP is given[3].

The grating has a spherical surface of radius R, thus all points, P, on the surface must satisfy the vertex equation for the sphere (*i.e.* the origin of the coordinate system is a point on the surface, the grating vertex[4]), which is

$$(R - u)^2 + w^2 + l^2 - R^2 = 0, \qquad (1.5a)$$

hence

$$u^2 - 2Ru + (w^2 + l^2) = 0. \qquad (1.5b)$$

Application of the formula for the roots of a quadratic equation yields

$$u = R \pm \{R^2 - (w^2 + l^2)\}^{1/2}. \qquad (1.6)$$

The positive value of the radical defines points on the opposite end of the diameter so only the negative value is significant. It is convenient to express equations (1.4) in terms of the distances between A, B and O and α and β, the angles of incidence and diffraction respectively. Hence cylindrical coordinates are introduced:

$$x = r\cos\alpha \qquad (1.7a) \qquad x' = r'\cos\beta \qquad (1.7b)$$

$$y = r\sin\alpha \qquad (1.7c) \qquad y' = r'\sin\beta. \qquad (1.7d)$$

Converting equation (1.4a) to cylindrical coordinates and substituting for u (equation (1.6) expanded in a power series) yields

$$|AP|^2 = (r - w\sin\alpha)^2 + w^2(\cos^2\alpha - \frac{r\cos\alpha}{R}) + l^2(1 - \frac{r\cos\alpha}{R})$$
$$- 2zl + z^2 + \frac{(w^2 + l^2)^2}{4R^2}(1 - \frac{r\cos\alpha}{R})(1 + \frac{w^2 + l^2}{2R^2} + \ldots.). \qquad (1.8)$$

The square root can be extracted by a further series expansion leading to the final expression. In order to simplify treatment of the series expansion, AP and BP are written as

[3] Namioka [4] showed that, although the introduction of the characteristic function (equation (1.1b)) is correct, the subsequent treatment of it by Beutler was, in some cases, incorrect, making some of his results incorrect. However, his results on the primary focusing conditions and the astigmatism of the concave grating remain perfectly valid (a mathematical justification of which is given in Namioka's paper). As these are the two main points of interest in this work, Namioka's corrections to Beutler's theory are therefore ignored.

[4] Normally the origin is at the centre of the sphere, the equation being $u^2 + w^2 + l^2 = R^2$.

$$AP = F_1 + F_2 + F_3 + \tag{1 9a}$$

$$BP = F_1' + F_2' + F_3' + \tag{1 9b}$$

so that the terms can be tabulated separately for more detailed examination in the following sections The terms, F_n, have individual physical significance with regard to image formation or its imperfections In general, successive terms exhibit decreasing order of magnitude due to successively higher inverse powers of R, r or r' Hence the higher order terms can generally be neglected For the purposes of this discussion, the optical path function can be written as

$$F = F_1 + F_2 + F_3 + F_1' + F_2' + F_3' + m\lambda w/d \tag{1 10}$$

where $$F_1 = r - w \sin\alpha \tag{1 10a}$$

$$F_2 = \frac{1}{2} w^2 \left(\frac{\cos^2\alpha}{r} - \frac{\cos\alpha}{R}\right) + \frac{1}{2} w^3 \frac{\sin\alpha}{r} \left(\frac{\cos^2\alpha}{r} - \frac{\cos\alpha}{R}\right) + \frac{1}{2} w^4 \frac{\sin^2\alpha}{r} \left(\frac{\cos^2\alpha}{r} - \frac{\cos\alpha}{R}\right) + \tag{1 10b}$$

$$F_3 = \frac{1}{2} l^2 \left(\frac{1}{r} - \frac{\cos\alpha}{R}\right) - l \frac{z}{r} + \frac{z^2}{2r} \tag{1 10c}$$

$$F'_1 = r' - w \sin\beta \tag{1 10d}$$

$$F_2' = \frac{1}{2} w^2 \left(\frac{\cos^2\beta}{r'} - \frac{\cos\beta}{R}\right) + \frac{1}{2} w^3 \frac{\sin\beta}{r'} \left(\frac{\cos^2\beta}{r'} - \frac{\cos\beta}{R}\right) + \frac{1}{2} w^4 \frac{\sin^2\beta}{r'} \left(\frac{\cos^2\beta}{r'} - \frac{\cos\beta}{R}\right) + \ldots \tag{1 10e}$$

$$F_3' = \frac{1}{2} l^2 \left(\frac{1}{r'} - \frac{\cos\beta}{R}\right) - l \frac{z}{r'} + \frac{z^2}{2r'} \tag{1 10f}$$

1.1.2 The grating equation

Isolating the first two terms and the last term of equation (1 10),

$$\begin{aligned} F &= F_1 + F'_1 + m\lambda w/d \\ &= r - w \sin\alpha + r' - w \sin\beta + m\lambda w/d \\ &= r + r' - w(\sin\alpha + \sin\beta) + m\lambda w/d \end{aligned} \tag{1.11}$$

Applying Fermat's principle ($\partial F/\partial w = 0$) gives

$$d\,(\sin\alpha + \sin\beta) = m\lambda. \tag{1.12}$$

This is the well-known plane diffraction grating equation which describes dispersion by a periodic set of lines separated by a distance d.

1.1.3 The Rowland circle focusing conditions

Obviously equation (1.12) cannot describe focusing by the grating as r and r' are not present. However, applying Fermat's principle to the second pair of terms in equation (1.10) gives

$$\begin{aligned}\frac{\partial(F_2 + F_2')}{\partial w} = w\left(\frac{\cos^2\alpha}{r} - \frac{\cos\alpha}{R} + \frac{\cos^2\beta}{r'} - \frac{\cos\beta}{R}\right)\\ + \frac{3}{2}w^2\left\{\frac{\sin\alpha}{r}\left(\frac{\cos^2\alpha}{r} - \frac{\cos\alpha}{R}\right)\right.\\ \left. + \frac{\sin\beta}{r'}\left(\frac{\cos^2\beta}{r'} - \frac{\cos\beta}{R}\right)\right\} + \ldots = 0\end{aligned} \tag{1.13}$$

As $w \neq 0$, the first member of equation (1.13) is zero if

$$\frac{\cos^2\alpha}{r} - \frac{\cos\alpha}{R} + \frac{\cos^2\beta}{r'} - \frac{\cos\beta}{R} = 0$$

and thus if

$$\cos^2\alpha/r = \cos\alpha/R \quad \text{and} \quad \cos^2\beta/r' = \cos\beta/R$$

giving $r = R\cos\alpha$ *(a)* and $r' = R\cos\beta$ *(b)* (1.14)

These solutions are the equations (in polar coordinates) of a circle of diameter R, with r and r' on the circle, that is, the Rowland circle. They are also solutions to the second term of equation (1.13). Indeed, it can be shown that all the higher terms in F_2 and F_2' cancel. This also applies to F_6 and F_6'[3] as well as to the partial differential, $\partial(F_6 + F_6')/\partial w$, thus the Rowland circle condition (equations (1.14)) reduces these expressions to zero. This shows ample justification for use of the Rowland circle. There are other terms which do not cancel under Rowland circle conditions, most notable of which are F_3 and F_3'. These and other terms describe the various imperfections (aberrations) which occur in the image. Of particular importance are astigmatism and the curvature of astigmatic spectral lines. Analysis of curvature and other aberrations will be omitted due to their complexity and the fact that they have relatively little bearing on the type of spectroscopic studies dealt with here.

1.1.4 Astigmatism

Astigmatism results in the source point being imaged as a vertical line. That is, horizontal focusing is complete but vertical focusing is only partially achieved on the Rowland circle, a secondary (vertical) focus (resulting in a horizontal line) being produced beyond the Rowland circle. A quantitative evaluation of the magnitude of astigmatism is as follows.

The point source at z, α and r is focused at z', β and r' if Fermat's principle of least time is fulfilled for $(F_3 + F_3')$ with respect to l, thus

$$\frac{\partial(F_3 + F_3')}{\partial l} = l\left(\frac{1}{r} - \frac{\cos\alpha}{R} + \frac{1}{r'} - \frac{\cos\beta}{R}\right) - \frac{z}{r} - \frac{z'}{r'} = 0 \qquad (1.15)$$

Introducing the Rowland circle conditions (equations (1.14)),

$$l\left(\frac{1}{R\cos\alpha} - \frac{\cos\alpha}{R} + \frac{1}{R\cos\beta} - \frac{\cos\beta}{R}\right) - \frac{z}{R\cos\alpha} - \frac{z'}{R\cos\beta} = 0 \qquad (1.16)$$

As $\quad 1/R\cos\alpha - \cos\alpha/R = (1 - \cos^2\alpha)/R\cos\alpha$

and $\quad 1/R\cos\beta - \cos\beta/R = (1 - \cos^2\beta)/R\cos\beta,$

knowing that $1/R \neq 0$ gives

$$l\left(\frac{\sin^2\alpha}{\cos\alpha} + \frac{\sin^2\beta}{\cos\beta}\right) - \frac{z}{\cos\alpha} - \frac{z'}{\cos\beta} = 0 \qquad (1.17)$$

Thus the length of the astigmatic image, z', is given by

$$z' = \left[z\,\frac{\cos\beta}{\cos\alpha}\right] + l\left(\sin^2\beta + \sin^2\alpha\,\frac{\cos\beta}{\cos\alpha}\right) \qquad (1.18)$$

This expression relates source length, z, and illuminated length of grating rulings, l, to image length, z'. The second term is independent of z, thus describing the astigmatism produced by a point source ($z = 0$). The dependence of this expression on α and β implies that the effect of astigmatism is greatest at grazing incidence. This is true of aberrations in general and is an unavoidable consequence of working with such large angles of incidence and diffraction.

Assuming that a point source in the plane of the Rowland circle ($z = 0$) will have its secondary focus in the plane of the circle ($z' = 0$), the location of the secondary focus can be deduced by writing equation (1.15) subject to those constraints ($z = 0$ and $z' = 0$), thus

$$l(1/r - \cos \alpha/R + 1/r' - \cos \beta/R) = 0 \qquad (1.19)$$

and since $l \neq 0$

$$1/r - \cos \alpha/R + 1/r' - \cos \beta/R = 0 \qquad (1.20)$$

where r' gives the location of the secondary focus. At this point it should be noted that due to the wavelength dependence of diffraction (equation (1.12)), both the primary and secondary foci have unique positions for each wavelength of incident radiation (of course in the case of the Rowland circle grazing incidence mount, all the primary focal positions lie along the Rowland circle).

1.1.5 Angular dispersion

The dispersion of a grating describes how the various wavelengths are distributed along the Rowland circle. Angular dispersion expresses this as the change in diffraction angle with a change in wavelength. This is evaluated by differentiating equation (1.12) with respect to wavelength, and, for a fixed angle of incidence, is given by $d\beta/d\lambda = m/d \cos \beta$.

1.1.6 Resolving power

Dispersion and resolving power are closely related, dispersion determining the separation of two wavelengths while resolving power determines whether this separation can be distinguished. Each dispersed and focused (monochromatic) beam forms a diffraction pattern having its own principal and secondary maxima. If we use Rayleigh's criterion, two lines of equal intensity will be resolved when the maximum of one falls on the minimum of the other. The angular distance between the principal maximum and its first minimum is called the angular half-width. This width provides a theoretical limit to the resolving power of a grating and, for a plane grating, is given by $\Delta\beta = \lambda/Nd \cos \beta$ [2]. The resolving power, P, is defined as $\lambda/\Delta\lambda$, where $\Delta\lambda$ is the minimum resolvable wavelength separation. Substituting the equation for the angular half-width into that for angular dispersion yields an expression for the resolving power which can be written as $P = mN$. It has been shown by Namioka [4] and Mack, Stehn and Edlen [6] (using physical optics) that the equation for the angular half-width used above does not apply to the concave grating as the diffraction minima do not reach zero. Thus they introduced a modified Rayleigh's criterion which did not require that the maximum of one line should fall on the first minimum of the other. It does require, however, that the ratio of the minimum intensity of the composite structure to that of either maximum is $8/\pi^2$ (0.8106), as it is in the Rayleigh definition (see figure 1.4 below).

Using this criterion, it can be shown from physical optics that $P = mN = Wm/d$ when

the illuminated width of the grating is less than some value, W. As this illuminated width is increased beyond W, the resolving power still increases, but not so rapidly as mN, reaching a maximum at $W = W_{opt}$. This optimum resolving power is then given by $P_{opt} = 0.92\ W_{opt}\ m/d$. By analysis of the fifth order terms [3] of the optical path function, an expression for W_{opt}, the optimum illuminated width of the grating, may be derived. This is a rather lengthy process so only the result is presented.

$$W_{opt} = 2.38[R^3\lambda \cos\alpha \cos\beta /(\sin^2\alpha \cos\beta + \sin^2\beta \cos\alpha)]^{1/4}. \qquad (1.21)$$

This expression gives the width of the grating which should be illuminated to optimise the resolving power of the system. This plays an important part when considering how the slit should be illuminated, as it acts as a source for the grating.

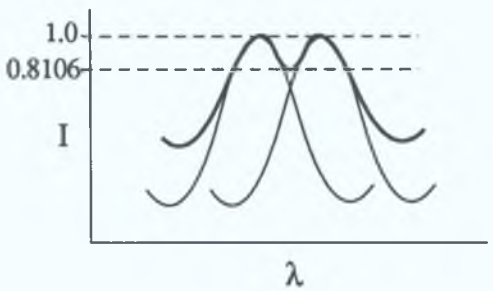

Figure 1.4. Plot of relative intensity against wavelength, showing the modified Rayleigh's criterion. (After Samson [2]).

1.1.7 Concluding remarks

Figure 1.5 shows a schematic representation of the focusing properties of the astigmatic grazing incidence mount. For a slit illuminated by a symmetrically diverging source, only a small fraction of the flux is admitted to the system. The slit length utilised (figure 1.5 (b)) and the width of the grating illuminated (figure 1.5 (a)) by such an arrangement depend very much on source position and geometry, which may not always be either well known or easily controllable. For sources of small size, as in the case of the laser plasma, the optimum width of the grating may not be filled and thus the grating's resolving power may not be optimised. This is best avoided by making the slit and grating illumination independent of source geometry or position, which can be achieved by the addition of a collecting/focusing element between source and slit.

Normally, the astigmatism can be tolerated as a slit is used as an effective source with parallel lines as images, giving similar optical performance to prism spectrographs. It does, however, result in two drawbacks of particular relevance to laser plasma studies: spreading the radiation over long spectral lines reduces the intensity of the lines and the inability of such a system to focus in the vertical plane excludes the utilisation of this plane for spatially resolved studies of the source. The high resolving power of modern gratings requires narrow slits,

further reducing line intensity. This, coupled with the analysis of short-lived sources compounds the astigmatic loss into a serious problem.

As Beutler concluded in 1942: "In general, it may be stated that the astigmatism is inherent in the concave mirror, which is the basis of the grating, as soon as the angle of incidence or diffraction is other than zero and that therefore no radical removal of it is possible, but only compensation by auxiliary optical elements."

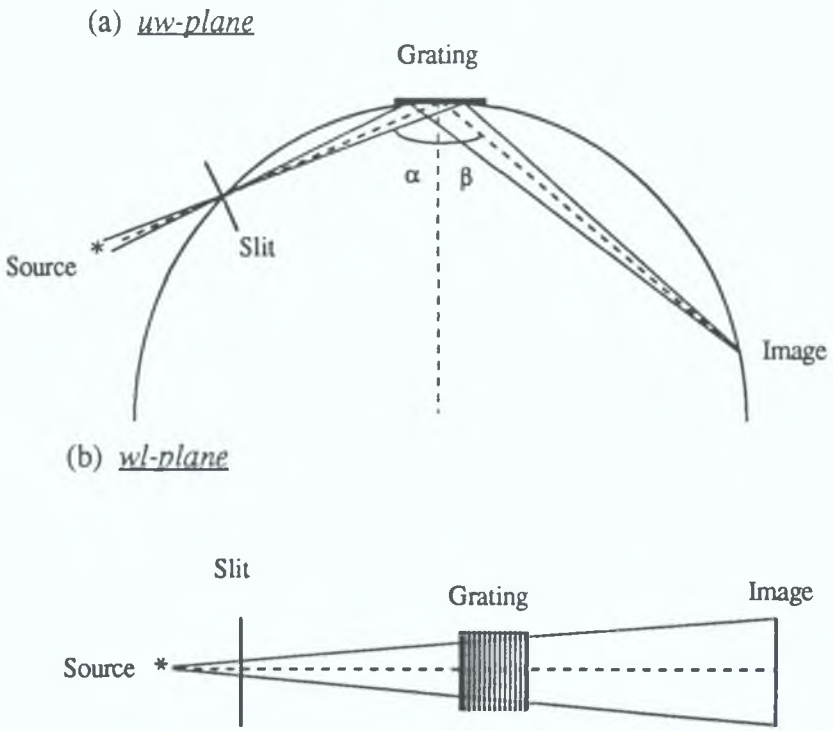

Figure 1.5. Focusing properties of the Rowland circle.

1.2 The toroidal mirror

The circular torus is generated by revolving a circle about a straight line lying in the plane of the circle (see figure 1.6). Hence the surface of a torus has two distinct radii of curvature, R (major radius) and ρ (minor radius), in the w and l planes respectively. A portion of the inside of the outer surface (centred on the origin in figure 1.6) replicated on a glass substrate produces a concave toroidal mirror. As demonstrated in the following sections (1.2.1 to 1.2.3), using geometric optics, the vertical and horizontal focusing properties of the toroidal mirror can be independently controlled by variation of the two radii (and the angle of incidence). The toroidal surface is also particularly simple to make in comparison to other non-spherical surfaces.

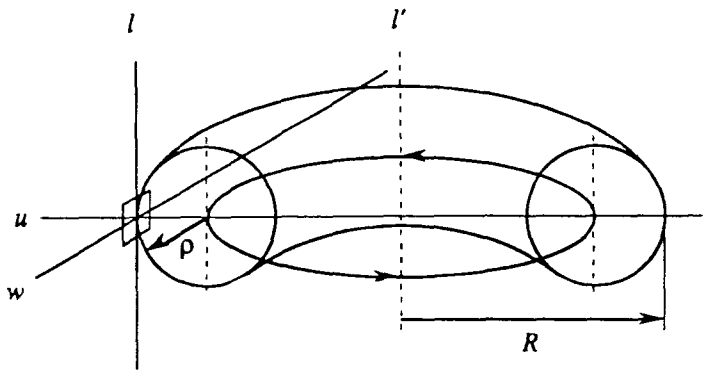

Figure 1 6 Generation of a torus

1.2.1 General theory

Soon after the publication of Beutler's description of the concave spherical grating, H Haber [7] applied the same technique to the analysis of the toroidal grating The optical path function, $F = AP + BP + m\lambda w/d$, is derived in the same way with the exception that the equation for the spherical surface (equation (1 5)) is replaced by the equation for the toroidal surface

$$u^2 + w^2 + l^2 = 2Ru - 2(R - \rho)\{R - [(R - u)^2 + w^2]^{1/2}\} \qquad (1\ 22)$$

In the case where $\rho = R$, this expression reduces to equation (1.5), the spherical case Expanding equation (1.4a) yields

$$|AP|^2 = (x - u)^2 + (y - w)^2 + (z - l)^2 \qquad (1.4a)$$

$$= x^2 + y^2 + z^2 - 2xu - 2yw - 2zl + u^2 + w^2 + l^2 \qquad (1\ 23)$$

where $x^2 + y^2 = r^2$

Expanding equation (1 22) in a power series and substituting into equation (1 23) yields the Cartesian expression for $[AP]^2$ In the spherical case, this substitution eliminated u directly (see equation (1 8)) In the present case, elimination of u requires the extraction of a quadratic equation in u and substituting the series expansion of the negative radical of the solution as before (see equation (1 6)) Conversion to cylindrical coordinates and extraction of the square root yields the final expression for $[AP]$ $[BP]$ is derived similarly The optical path function, $[AP] + [BP]$, after grouping the terms by their power of w or l, can be written as shown (see equation (1 24) below)

As Beutler demonstrated for the expression pertaining to the spherical grating, the

terms, T_n, of (1 24) have individual physical significance for image formation and its imperfections The higher order terms, describing aberrations, are omitted for simplicity as this discussion is concerned mainly with the focusing conditions Imaging imperfections are more accurately quantified using ray-tracing techniques which will be dealt with in subsequent chapters T_1 relates to the general grating equation, T_2 describes the primary (horizontal) focus and T_3 describes the secondary (vertical) focus produced as a result of astigmatism

Although (1 23) pertains to a toroidal grating, setting $\alpha = \beta$ invokes the law of reflection, thus describing a toroidal mirror, the focusing conditions of which are described by T_2 and T_3 These conditions are derived by applying Fermat's principle as before (see equations (1 2)), *i e* the condition for a true focus requires that the partial derivatives of the terms of the optical path function equal zero

$$AP + BP = r + r' - (\sin\alpha + \sin\beta)w \qquad (T_1)$$

$$+\frac{1}{2}\left(\frac{\cos^2\alpha}{r} - \frac{\cos\alpha}{R}\right)w^2 + \frac{1}{2}\left(\frac{\cos^2\beta}{r'} - \frac{\cos\beta}{R}\right)w^2$$

$$+\frac{1}{2}\frac{\sin\alpha}{r}\left(\frac{\cos^2\alpha}{r} - \frac{\cos\alpha}{R}\right)w^3 + \frac{1}{2}\frac{\sin\beta}{r'}\left(\frac{\cos^2\beta}{r'} - \frac{\cos\beta}{R}\right)w^3$$

$$+\frac{1}{2}\frac{\sin^2\alpha}{r}\left(\frac{\cos^2\alpha}{r} - \frac{\cos\alpha}{R}\right)w^4 + \frac{1}{2}\frac{\sin^2\beta}{r'}\left(\frac{\cos^2\beta}{r'} - \frac{\cos\beta}{R}\right)w^4 \qquad (T_2)$$

$$+\frac{1}{2}\left(\frac{1}{r} - \frac{\cos\alpha}{\rho}\right)l^2 + \frac{1}{2}\left(\frac{1}{r'} - \frac{\cos\beta}{\rho}\right)l^2 + \frac{1}{2r}[z^2 - 2lz] + \frac{1}{2r'}[z'^2 - 2lz']$$

$$+\frac{1}{8r}\left\{\left(\frac{1}{r} - \frac{\cos\alpha}{\rho}\right)l^2 + \frac{1}{r}[z^2 - 2lz]\right\}^2$$

$$-\frac{1}{8r'}\left\{\left(\frac{1}{r'} - \frac{\cos\alpha}{\rho}\right)l^2 + \frac{1}{r'}[z^2 - 2lz]\right\}^2 \qquad (T_3)$$

(1 24)

1.2.2 Primary focus

T_2 has terms in w^2, w^3 and w^4, thus Fermat's principle requires that

$$\partial T_2/\partial w = \partial/\partial w(A(w^2) + B(w^3) + C(w^4)) = 0,$$

which implies that

$$\partial A/\partial w = 0, \quad \partial B/\partial w = 0 \quad \text{and} \quad \partial C/\partial w = 0.$$

For small values of w (which is generally the case as the w axis is along the width of the mirror), the higher order terms have small numerical values and may be neglected. Thus

$$T_2 = \frac{1}{2}\left(\frac{\cos^2\varphi}{r} - \frac{\cos\varphi}{R}\right)w^2 + \frac{1}{2}\left(\frac{\cos^2\varphi}{r'} - \frac{\cos\varphi}{R}\right)w^2$$
$$= \frac{1}{2}\left\{\cos\varphi\left(\frac{1}{r} + \frac{1}{r'}\right) - \frac{2}{R}\right\}\cos\varphi\, w^2 \qquad (1\ 25)$$

where $\alpha = \beta = \varphi$ The condition for a focus is given by setting the partial derivative of equation (1 25) with respect to w equal to zero,

$$\frac{\partial T_2}{\partial w} = \left[\cos\varphi\left(\frac{1}{r} + \frac{1}{r'}\right) - \frac{2}{R}\right]\cos\varphi\, w = 0$$
$$\text{thus} \quad \frac{1}{r} + \frac{1}{r_1'} = \frac{2}{R\cos\varphi} \qquad (1\ 26)$$

This equation defines the location of the primary focus, r'_1

1 2.3 Secondary focus

To simplify the analysis of T_3 for the purpose of obtaining an expression for the location of the secondary focus, it is assumed that for a point source on the equatorial (uw) plane, the focus will also lie on that plane. Thus both z and z' are zero. The squared terms in T_3 can also be neglected, so T_3 can be written as

$$T_3 = \frac{1}{2}\left\{\left(\frac{1}{r} + \frac{1}{r'}\right) - \frac{2\cos\varphi}{\rho}\right\}l^2 = 0 \qquad (1.27)$$

and the condition for a focus is given by setting the partial derivative equal to zero as before,

$$\frac{\partial T_3}{\partial l} = \left(\frac{1}{r} + \frac{1}{r'} - \frac{2\cos\varphi}{\rho}\right)l = 0$$
$$\text{thus} \quad \frac{1}{r} + \frac{1}{r_2'} = \frac{2\cos\varphi}{\rho} \qquad (1\ 28)$$

where r'_2 is the location of the secondary focus.

1 2.4 Concluding remarks

By inspection of equations (1 26) and (1 28) it may be stated that for any given source distance, r, the locations of the primary and secondary foci, r'_1 and r'_2 respectively, can be independently controlled by selecting suitable values for the two radii, the major radius controlling the primary focus and the minor radius controlling the secondary focus, and the angle of incidence, which affects their positions relative to each other Figure 1 7 shows a schematic illustration of the focusing properties of the toroidal mirror, showing the formation of the two foci orthogonal to each other

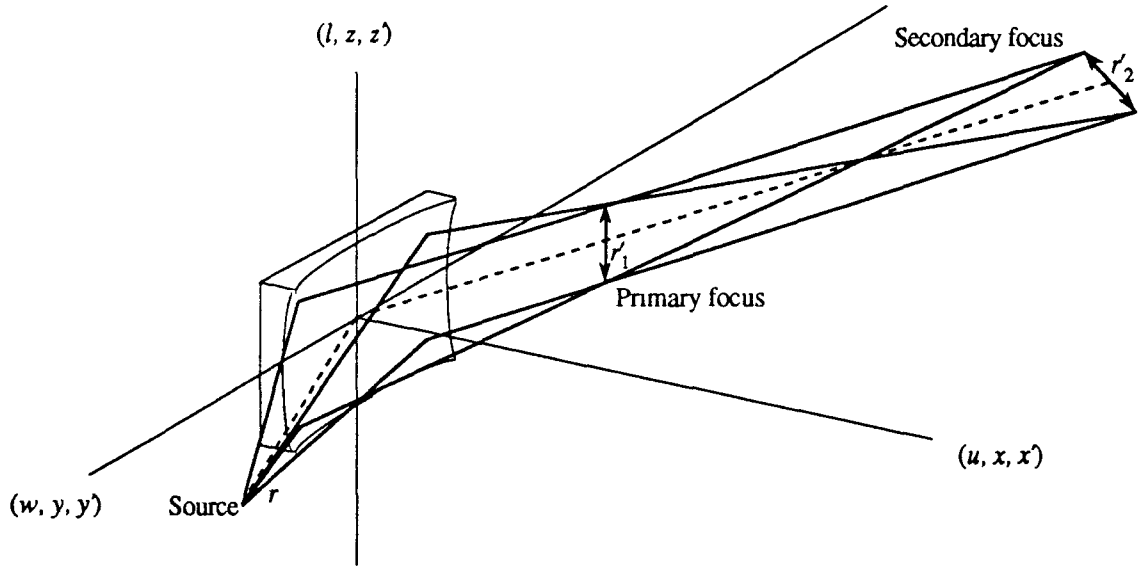

Figure 1.7. Focusing properties of the toroidal mirror.

As in the case of the spherical grating, a description of the imaging aberrations of the toroidal mirror may be derived by a more complete analysis of the optical path function. While such analyses are beyond the scope of this work, the main aberrations are now briefly discussed.

1 The primary image has the form of a parabolic curve in the plane perpendicular to the principal ray, the latter passing through its vertex The curvature of the image depends only on R, p, ρ and φ The image has a finite width, due mainly to spherical aberration of the mirror, which is minimised when $p = p' = R \cos \varphi$ [8].

2 The secondary image is also curved but, while being perpendicular to the primary image, is not perpendicular to the principal ray It is inclined at some angle to the perpendicular which is a function of the system aperture and the angle of incidence on the mirror. This inclination is most pronounced at grazing incidence.

Since the analytical treatment of aberrations leads to rather approximate results, no attempt to quantify the aforementioned aberrations is made at this stage. Chapters two and

three include optical characterisation of the system, before and after modification respectively, using ray-tracing methods This facilitates more accurate examination of the aberrations

1.3 High speed imaging: mirror and grating in series

To improve the efficiency (or speed) of a grazing incidence spectrograph requires that the losses outlined in section 1 1 7 be compensated for Thus the three main improvements are reducing astigmatism to concentrate the light in shorter, more intense spectral lines, coupling light into the spectrograph by focusing it onto the slit, optimising grating resolution by filling its optimum width Furthermore, if the astigmatism is correctly compensated for, the resultant spectra will be stigmatic (*i e* a point on the object plane being imaged as a point on the image plane) at some chosen wavelength Thus the source will be spatially resolved along the direction of the slit

The method by which the above aims are achieved using a toroidal mirror is now discussed It was originally developed by W A Rense and T Violett to increase the speed of a grazing incidence spectrograph, and later refined by G Tondello to produce stigmatic observations of laser-produced plasmas (see Introduction, p 3)

1.3.1 Method

Production of a stigmatic image on the Rowland circle requires that both the primary and secondary images produced by the grating (see sections 1 1.3 and 1 1 4) be formed on the circle. This is automatically fulfilled for the primary image (equation (1 14a)) if the effective source lies at r (on the Rowland circle), thus requiring only modification of the secondary focal conditions.

The condition that the secondary focus of the grating also lies on the Rowland circle is obtained by imposing $r' = R \cos \beta$ (equation (1 14b)) into equation (1 20) and rearranging to get

$$r_v = \frac{R}{\cos \alpha - \sin \beta \tan \beta} \qquad (1\ 29)$$

where r_v is the *secondary* effective source distance from the grating The term "secondary" is introduced as the separate manipulation of the primary and secondary foci (to force them to coincide at the Rowland circle) requires a separate effective source for each focus This is fulfilled for the primary image (the horizontally focused spectral line of the astigmatic system) by the vertical slit (a horizontally divergent line source) Thus to produce the secondary image (vertical focus) on the Rowland circle requires that a vertically divergent line source lies at the position defined by r_v.

At grazing incidence the denominator of (1 29) is negative, producing negative values

of r_v. This indicates that the effective source must be virtual, located behind the grating (see figure 1 8 (a)) So the focusing element must be inserted between source and entrance slit such that it produces a horizontal focus on the slit, to maximise the flux coupled into the system, and a vertical focus at r_v. Thus the foci act as the required line sources

The resolved focusing properties of the toroidal mirror are ideally suited to such requirements positioning its primary or horizontal focus on the slit and its secondary or vertical focus at r_v fulfills the above conditions (see figure 1 8)

It is clear from equation (1 12) that, at fixed angle of incidence on the grating, each wavelength has a unique position on the Rowland circle, thus r_v is wavelength dependent This implies that the stigmatic focusing conditions described above can only be strictly fulfilled for a single wavelength Thus a central wavelength in the region of interest must be selected From this, r_v is calculated and a toroidal mirror with suitable focusing properties can be designed

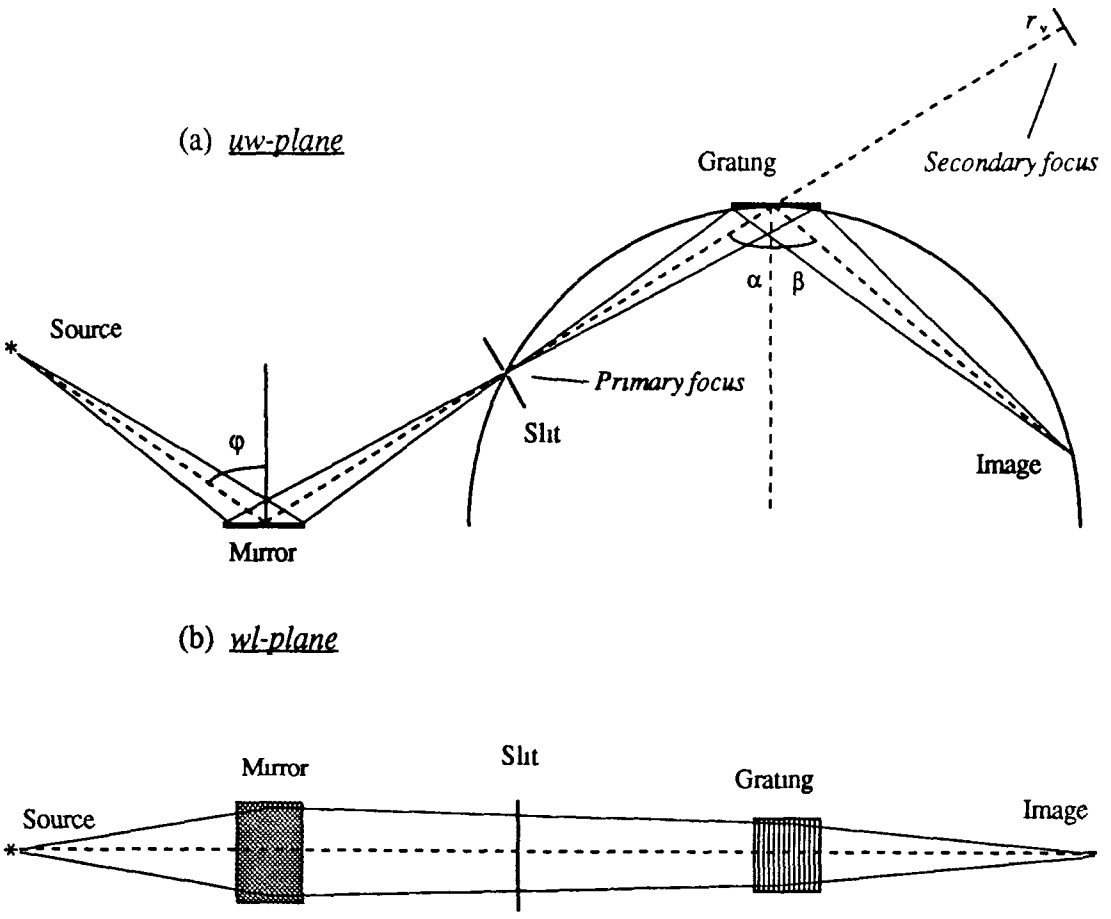

Figure 1.8 Configuration of toroidal mirror and spherical grating in series to compensate for astigmatism

Thus reduction/elimination of astigmatism is achievable, as is focusing the light through the slit. The final consideration is that of filling the optimum width of the grating. As the principal mirror parameters are determined by the required focusing conditions, with angle

of incidence being determined by the shortest wavelength of interest, as in the case of the grating (see section 3 1 1), the mirror width is used to ensure optimum grating illumination. By inspection of the geometry (figure 1 8 (a)), it is clear that a simple relationship exists between mirror width and grating illuminated width This relationship can be expressed as

$$w_{uw} = W_{opt}\, r'_1 / R \cos\varphi \qquad (1\ 30)$$

where w_{uw} is the mirror width in the uw plane So the width of the mirror in the uw plane must be calculated to produce optimum illumination of the grating, filling the aperture of the spectrograph and maximising spectral resolution.

1.3.2 Concluding remarks

The net result is the series arrangement of a toroidal mirror and a spherical diffraction grating in an XUV spectrograph which is capable of stigmatic imaging at a single wavelength and quasi-stigmatic imaging (or reduced astigmatism) in the neighbouring spectral region, as will be shown both by ray-tracing and experiment in subsequent chapters

References

1. Rowland, H A , Phil Mag , 13, 469 (1882).
2. Samson, J. A , *"Techniques of Vacuum Ultraviolet Spectroscopy"*, Wiley & Sons (1967).
3. Beutler, H G , J Opt Soc Am , 35, 311 (1945)
4 Namioka, T , J Opt Soc Am , 49, 446 (1959)
5 Born, M and Wolf, E , *"Principles of Optics"*, Pergamon Press, 6th Ed. (1980).
6 Mack, J E , Stehn, J R and Edlen, B , J Opt Soc Am , 22, 245 (1932)
7. Haber, H., J. Opt Soc Am , 40, 153 (1950)
8 Tondello, G , Optica Acta, 26, 357 (1979)

Chapter 2

The astigmatic dual laser-plasma experiment

This chapter describes the apparatus and techniques used to produce astigmatic photoabsorption spectra of the radiation emitted by laser-produced plasmas, *i.e.* the unmodified DLP experiment as used before the work described in this thesis was completed. This has been described in detail by J. Brilly [1] so this treatment is brief. By way of introduction, a general description of the equipment and experimental techniques employed is first presented. This is followed by a more detailed description of the system's components. The optics of the system are then characterised by ray tracing.

2.1 General description

The main elements of the experimental apparatus and method are common to both the modified and unmodified systems, so this and the following sections describe the main features of both, the differences introduced to improve the optical system being detailed in the following chapter.

2.1.1 Experimental apparatus

Plasma generation was carried out using two electronically synchronised, Q-switch pulsed solid state lasers, a ruby laser and a neodymium:YAG laser. The optical pulses produced were focused onto the surfaces of two metal targets by two plano-convex lenses. The target materials (in rod or disk form) were mounted in target holders on the end of drive shafts in an evacuated chamber (the target chamber), the laser light being admitted by a glass window. The drive shafts passed through seals in the chamber wall thus allowing rotation of the targets to provide a fresh surface for repeated plasma production. Stepper motors were attached to the target drive shafts to facilitate automatic target movement. This was controlled by a microcomputer which triggered the laser system and then rotated the targets, repeating this process a programmed number of times. The target chamber was mounted on the front of a grazing incidence spectrograph, of 2 metre grating radius, in front of the slit. Positioning of the plasmas was aided by a low power Helium-Neon (HeNe) laser mounted on the chamber such that it passed along the spectrograph axis.

The spectrograph consisted of three components an adjustable slit, which acted as an effective source, a concave diffraction grating, to disperse the radiation into its energy spectrum, a photographic plate mounted in a plateholder to record the focused spectrum These three independently adjustable components were positioned to lie exactly along the Rowland circle of the grating (the plateholder was shaped to clamp the glass photographic plates along the curvature of the Rowland circle) and were contained within a vacuum chamber To facilitate the recording of multiple spectra on one plate, a mask was fitted between the grating and plateholder This blocked all but a short portion of the long spectral lines The mask was moved across the beam by means of a slide which passed through the tank wall

Both chambers (target and spectrograph) were evacuated using a two-stage pump system consisting of a turbomolecular pump backed by a double-stage rotary pump This system pumped down to a working pressure of about 10^{-2} Pa (10^{-7} Atmospheres) in about twenty minutes, the pressure being read by a Penning ionisation gauge (see section 3 2 4) positioned close to the turbo pump

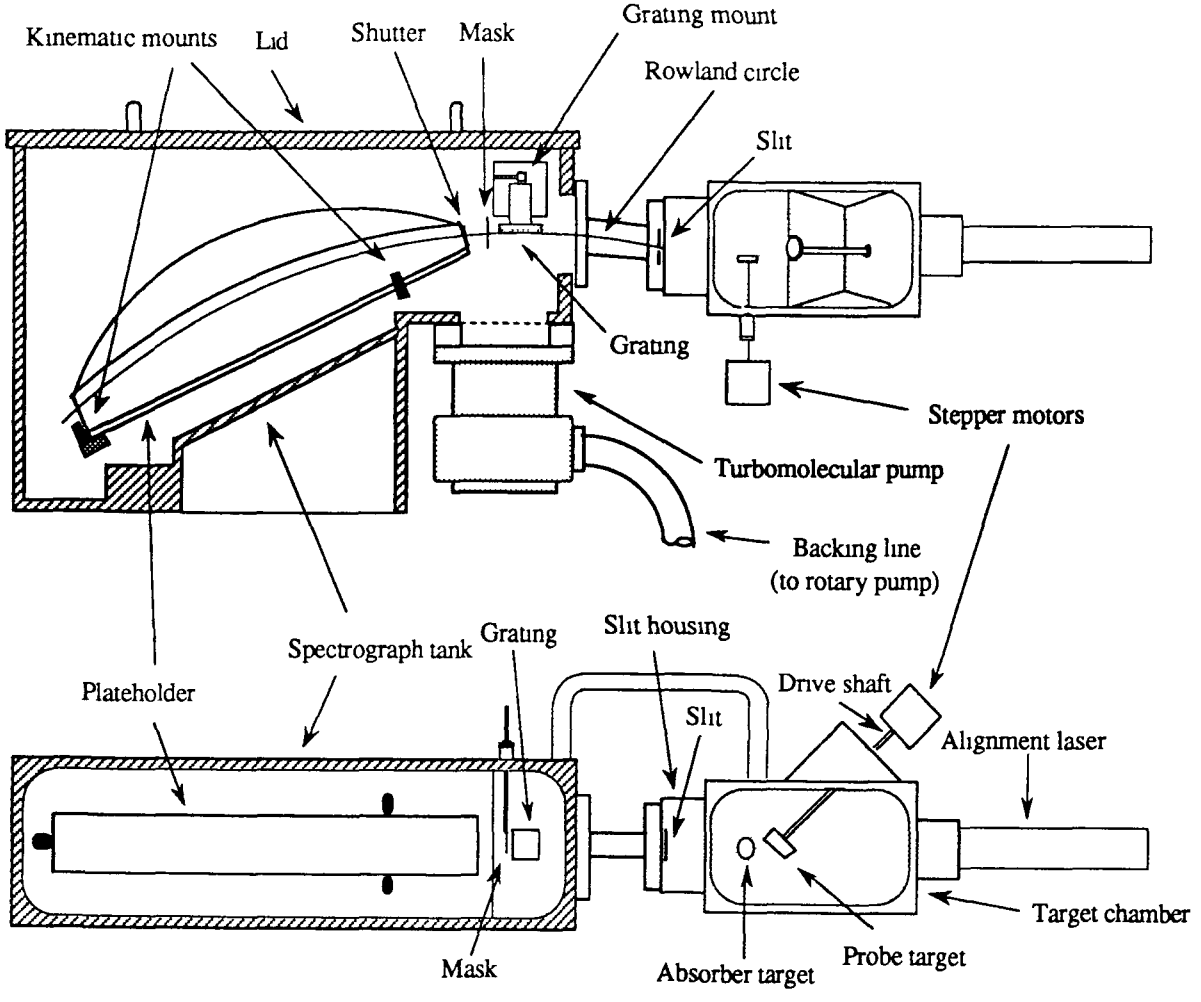

Figure 2 1. Schematic of the experimental apparatus

2.1.2 Experimental method

A schematic representation of the apparatus is shown in figure 2 1 The procedure involved in running a DLP photoabsorption experiment using this apparatus was as follows

1 The targets were positioned in the chamber with the lasers and focusing lenses aligned outside the chamber so that the plasma positions lay on the spectrograph axis The probe plasma was typically generated on tantalum (Ta) as this produces a virtually line-free continuum, with the absorbing plasma generated on some other metal

2 A photographic plate was loaded into the plateholder in low light conditions The plateholder was then placed in the spectrograph, secured by spring-clips to its correct position The plateholder featured an externally controlled shutter which prevented accidental exposure of the plate before commencement of the experiment

3 The system was evacuated by simply switching on the pump controller The two pumps were then under automatic control

4 A suitable inter-plasma time delay was programmed (see section 2 2 3) into the synchronisation electronics This was checked by firing the lasers onto a diffusing surface (*e g* a sheet of paper), detecting the pulses with a photodiode and measuring the peak to peak time difference (Δt) on a digital storage oscilloscope

5 The target controller (microcomputer) was programmed with the required number of laser shots and target rotations (typically the probe target was rotated after 5 laser shots and the absorber after 1 to 20, depending on target material). The experiment was effectively ready to run at this stage, requiring only a keystroke to commence execution (assuming the plate shutter had been opened and the mask positioned)

6 Having run the experiment, all that remained was to vent the vacuum system (switching off the pump controller initiated automatic venting) and to remove and develop the exposed plate in safe light conditions

2.2 The synchronised laser system

Both lasers used were commercially available, liquid cooled, Q-switch pulsed solid state lasers They were of a standard design where the laser cavity formed an optical bench mounted on a sturdy plinth and housed in a metal case, the controlling electronics and cooling systems were separately housed in a control unit The two were connected by a set of wires and pipes known as the umbilical

The synchronising electronics were custom designed and built. They featured a multi-channel digital delay system, with 10 ns resolution, based on commercially available programmable time delay modules. The main components of the laser system are now described in more detail

2 2.1 The ruby laser

The ruby laser was a standard JK Lasers System 2000, operated in Q-switch mode The laser consisted of a single oscillator which produced an output of approximately 1J in 35 ns (FWHM)[5] at 694 nm The lasing medium, ruby, was a crystal of aluminium oxide (Al_2O_3) in which some of the Al^{3+} ions were replaced by Cr^{3+} ions. Figure 2 2 shows a schematic of the ruby laser head An alignment HeNe was mounted on the back of the laser head to facilitate positioning of the laser without firing The crystal was optically pumped by high voltage xenon flashlamps Q-switching was achieved using a polariser and Pockels-cell combination as an electro-optical shutter Application of a voltage to the Pockels-cell closed the shutter during the initial stages of pumping As the energy stored in the ruby reached a maximum, the voltage was removed, opening the shutter and allowing a high-power pulse of short duration to be produced

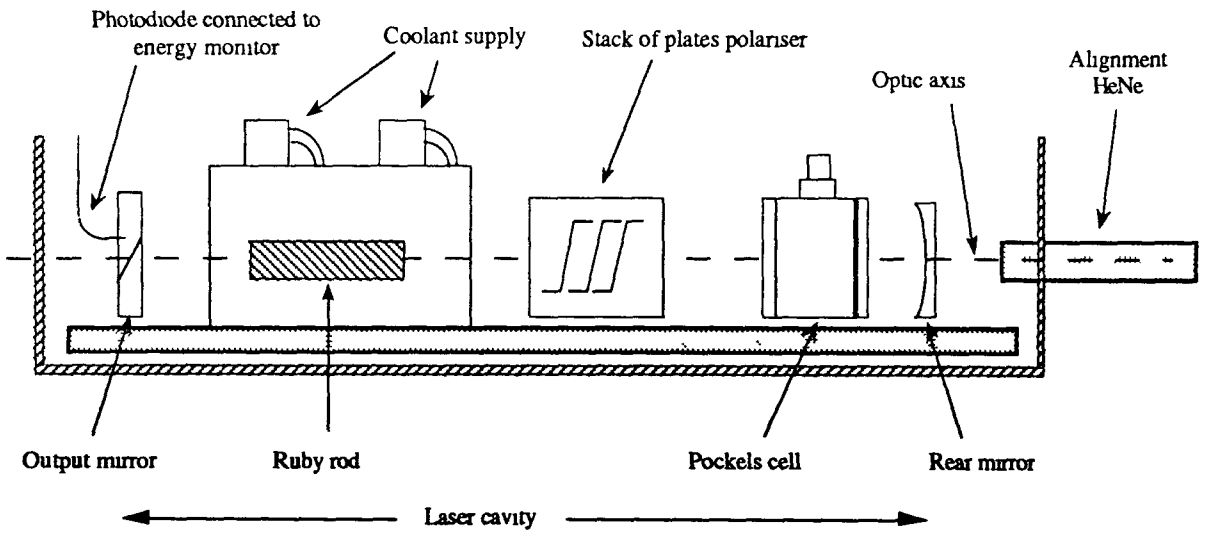

Figure 2.2. Schematic of the ruby laser head (after Evans [2])

2.2.2 The Nd YAG laser

The YAG laser was a Spectron Laser Systems SL 800 The laser material, neodymium-doped yttrium aluminium garnet (YAG), was a crystal of $Y_2Al_5O_{12}$ in which some of the Y^{3+} ions were replaced by Nd^{3+} ions The laser head featured a two-stage oscillator/amplifier system which had an output of approximately 1 J in 15 ns (FWHM) at a wavelength of 1064 nm Figure 2 3 shows a schematic of the YAG laser head. An alignment HeNe was mounted as shown Pumping and Q-switching were achieved as described for the ruby laser (see section 2 2 1 above)

[5] Full width at half maximum.

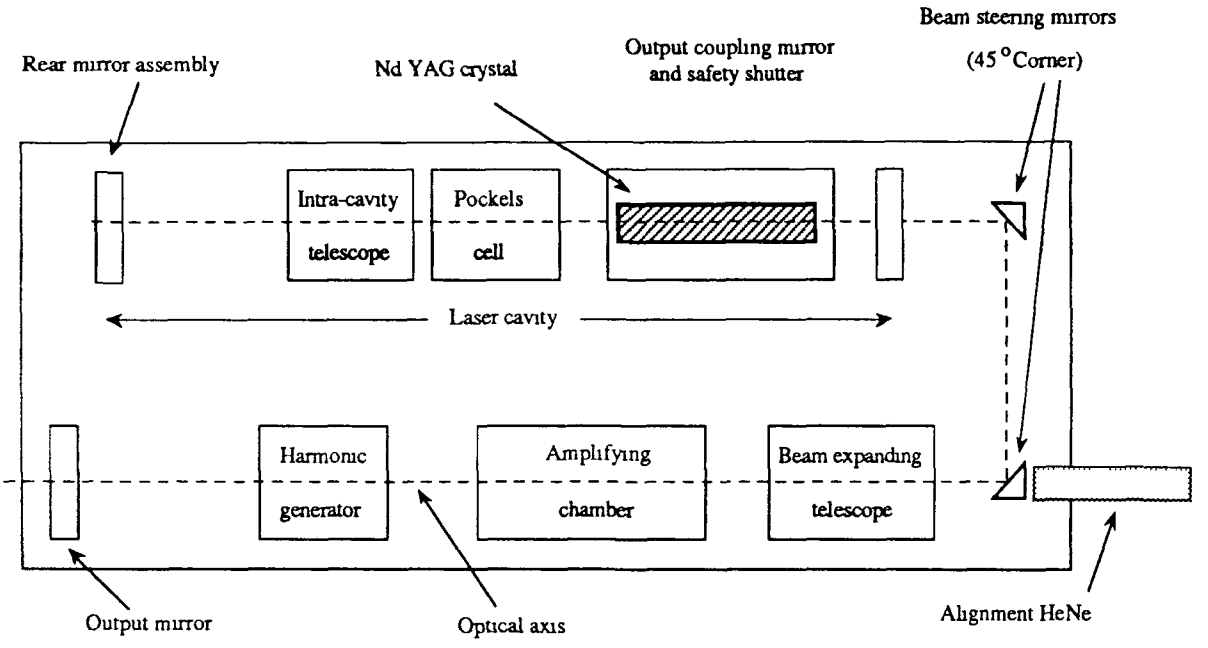

Figure 2 3. Schematic of the YAG laser head (after Evans [2])

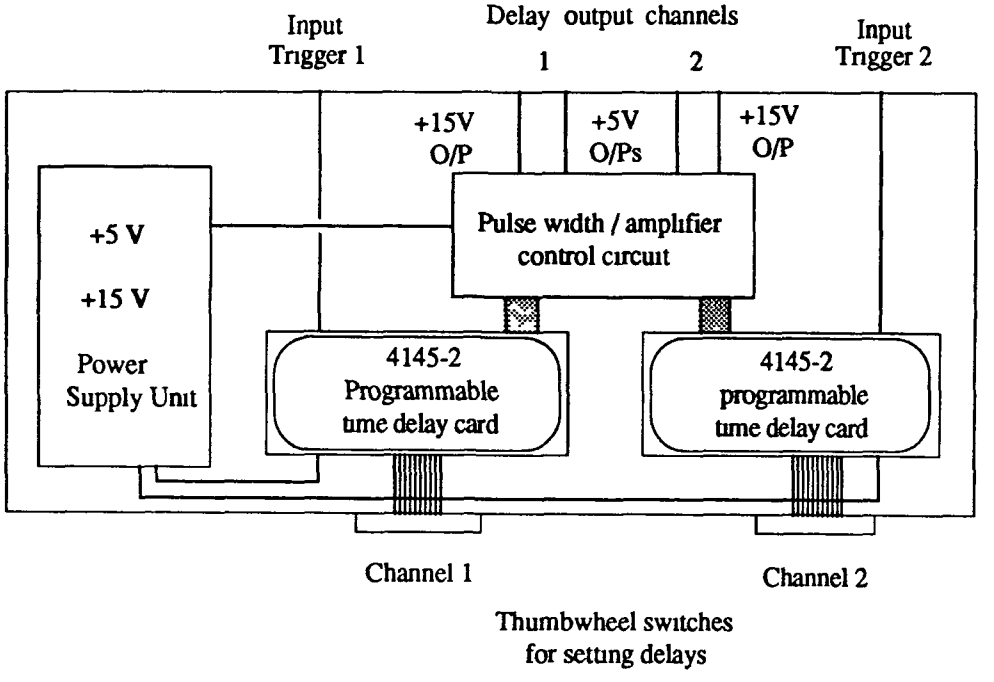

Figure 2.4. Schematic of two-channel delay generator (after Evans [2])

2 2.3 The delay generators

Laser synchronisation was achieved using a multichannel digital delay system based on a commercial programmable time delay module, the Evans Electronics 4145-2 This card featured an on-board crystal oscillator to establish an accurate timebase and a programmable delay range of 0 to 999 99 μs in increments of 10 ns All inputs and outputs were TTL[6] compatible with a maximum jitter of ±3 ns in the output

Delay programming was facilitated by thumbwheel switches arranged in five decades The output signals were buffered to provide the choice of +5 V or +15 V pulse height required for compatibility with the laser control units Figure 2 4 shows a schematic of the two channel delay unit. Two such units were constructed providing four controllable delay channels Radio frequency interference (RFI) and mains noise were eliminated by enclosing the system in a shielded case with the inputs and outputs fitted with decoupling capacitors

2.3 The spectrograph

The instrument used throughout this work was a 2 m grazing incidence spectrograph model E580, supplied by Hilger and Watts It was designed to cover a spectral range of 0 5 nm to 95 nm in the first spectral order, depending on the grating fitted Figure 2 1 includes a schematic diagram of the instrument The components of the spectrograph were as follows

2.3.1 The grating

The dispersing element was a platinum-coated, spherically concave grating with a radius of curvature of 2 m, supplied by Bausch and Lomb. It used the Rowland circle grazing incidence grating mount. The substrate dimensions were 35 x 45 x 10 mm with a ruled area of 25 x 35 mm It was ruled with 1200 lines per mm and a blaze angle of 1° 47'. The resultant spectral range was about from 0 5 nm to 50 nm with a dispersion of about 0 1 nm per mm at 12 nm on the Rowland circle

2.3.2 The entrance slit

The entrance slit formed a narrow aperture on the Rowland circle which acted as a line-shaped source for the grating It consisted of two independently adjustable jaws mounted on a stainless steel flange which facilitated connecting the spectrograph to the target chamber The slit assembly controlled the angle of incidence, so one of the jaws remained in a fixed position For the slit used, the angle of incidence is 86° Two alternate slit assemblies were available, having angles of 88° and 89° respectively The slit jaws were precision mounted so that they

[6] Transistor-transistor logic

were effectively vacuum sealed, the gas flow through the slit being negligible for a small slit width (a slit width of around 10-15 μm was used for the work described in this thesis). A pre-grating slit was positioned between entrance slit and grating. This prevented the number of grating rulings illuminated from exceeding the optimum.

2.3.3 The detector

The radiation detector consisted of an XUV sensitive photographic plate bent along the Rowland circle by the plateholder.

The plateholder consisted of two main components, both made from the same material as the tank (see section 2.3.4). The plateholder body had two ridges that position the emulsion-coated side of the plate along the Rowland circle, a curved surface machined to a positional accuracy of 5 μm. The plate was pressed into place by rubber cords on the underside of the lid, which was itself secured by screw-clamps. The plateholder was positioned in the tank by means of a three point kinematic support and spring-loaded clips.

The spectra were recorded on Kodak™ SWR[7] glass photographic plates, the dimensions of which were 0.71 x 51 x 254 mm (0.28 x 2 x 10 in).

2.3.4 The vacuum tank

The grating mount and plateholder were both mounted inside the tank, with the slit assembly bolted onto the tank via a sealed flange. Access to the interior of the vessel was by a removable lid made from 12.5 mm aluminium alloy plate which is sealed by a rubber O-ring.

The vacuum tank was a magnesium-zirconium alloy casting. Chosen for its good vacuum compatibility, this alloy is also very light. The tank was shaped to reduce internal volume and ribbed to eliminate distortion under vacuum. It also featured a flange in front of the grating for connection to the pumping system.

2.4 The target chamber

The experimental chamber was machined from a solid piece of mild steel. Two sides were completely open, being vacuum sealed by glass plates held against O-rings (see figure 2.1). This allowed maximum visibility for the purpose of alignment and also monitoring plasma formation during experiments. The probe target was mounted through the back plate at 45° to the spectrograph axis and the absorbing target was mounted through the bottom, normal to the axis. The drive shafts passed out of the chamber through Wilson seals. These were designed to allow rotation and translation without leaking. The chamber also featured a laser-cradle attachment and a window at the back for mounting the alignment HeNe, and a standard vacuum connection to the spectrograph tank to equalise chamber pressures.

[7] Short wave radiation.

2.5 The optical system

The optical theory governing the imaging characteristics of the system is given in section 1.1. Due to the complex nature of geometrical modelling in terms of a characteristic function, many simplifying assumptions must be made if numerical calculations for a specific system are to be undertaken. This limits the usefulness of such descriptions and also is compounded by the errors inherent in the evaluation of the trigonometric functions. Alternatively, the path of individual photons (rays) may be accurately determined with the help of elementary geometry and the successive application of the laws of reflection, refraction or attenuation. This method is known as ray-tracing. The optical system was thus modelled using Shadow, a ray-tracing computer package.

2.5.1 Shadow: an XUV ray tracing program

Shadow is a software package developed under the direction of F. Cerrina [3] to study the propagation of a photon beam through an optical system. The program is general, but is optimised for the case of soft x-rays and reflective optics such as those encountered in the XUV. It is written in Fortran 77 and runs under VMS on a DEC VAX 6230 in double precision (with a typical accuracy of 1 in 10^{13}). No approximations are made and the use of trigonometric functions is kept to a minimum by vector algebra.

The program treats an optical system as a series of optical elements, each one defined by a reflecting or refracting surface. Each optical element is delimited by two planes, the object (source) plane and the image plane. The image plane of a given optical element is the object plane of the following one. The main program, Shadow, traces up to 5000 rays through a system in this way, generating a series of output files which are analysed by utility programs. The utilities range from simple code to translate the output files into a useful format to scaled, on-screen plotting routines for graphical analysis.

2.5.2 System modelling

Shadow data could be entered in one of three ways: Prompt mode (in which the user answers questions from Shadow designed to cover the full specification of a source or optical element); Menu mode (where the program generates a command level through which a set of menus were accessed); Batch mode (where a parameter file generated by a previous input session is supplied to Shadow for a re-run). Menu mode proved to be the most versatile and was thus used throughout this work.

The data to characterise an optical system were entered in two separate modules within Shadow's menu mode command level, called SOURCE and TRACE respectively. The source description was entered in the SOURCE module and the optical system parameters were entered

in the TRACE module

On entering SOURCE, a menu tree was set up to facilitate data input The structure of this was as follows[8] Sub-menus are denoted by indentation, actual data are included as examples No lengths or positions were dimensioned (unless otherwise indicated), so consistency of units was essential

```
SOURCE 1

-------------------------------------------------------------

File to store rays        BEGIN1
Source type               Random
# rays                    5000
Spatial type              Ellipse
      Width        (X)·          0 125
      Height       (Z)           0 125
      Depth        (Y)           Off
Angle distribution        Uniform
      Divergences (in Radians)
      Horizontal   (X+)          1 0 E-1
                   (X-)          1 0 E-1
      Vertical     (Z+)          3 0 E-3
                   (Z-):         3.0 E-3
Photon energy dist :      Multi Line
      Units.                     Ångstroms
      # lines                    2
      At energy    (1)           168
                   (2)           130
```

Note that the coordinate system referred to here is that of Shadow It is related to that of chapter 1 by $x = l$, $y = w$ and $z = u$

This information could be saved as text, for future use or modification, under a user-defined file name (as with all source files, it was given a 00 extension) On exiting from SOURCE, the data entered was stored in a parameter file called START 00 The parameter file was used to generate a binary output file (double precision array) which described the collection of rays constituting the source, called BEGIN DAT as specified in the main menu (by changing this file name, various sources can be prepared without having to store the rather large text and parameter files)

[8] For the sake of brevity, irrelevant menu structures are omitted.

On entering TRACE, a similar menu tree was set up for inputting the optical system parameters Once in TRACE, each optical element or screen had to be separately defined, numbered and the necessary data entered Again, the information could be saved as text under a user-defined file name, with the optical elements saved separately using their numbers as file extensions, *i e* 01, 02, etc The data required to define the grating was as follows

```
OPTICAL ELEMENT 1

-------------------------------------------------------------------

Source file name          BEGIN
Source plane distance     199 51
Image plane distance      0
Angle of incidence        86
Angle of reflection       0
Type of element           Reflector
Figure                    Spherical
      Mirror parameters
            Foci and continuation
            planes.             Coincident
            Radius of curv      2000
      Surface curvature.        Concave
      Limits check:
            Shape·              Rectangle
            Dimensions  X(+): 12.5
                        X(-). 12 5
                        Y(+)· 17 5
                        Y(-)  17 5
Diffraction               Grating
      Ruling type         Constant
      Lines/cm            12000
      Autotuning·         Yes
      Diffr  order.       -1
      Wavelength.         168 Å
      Mount type          ERG
```

The angle of reflection (or diffraction, as it was in this case) and the image plane distance were set to zero so that when autotuning was selected (from the sub-menu of "diffraction") they were calculated by ray-tracing methods.

The second optical element represented the photographic plate. This was achieved by setting up a sphere of radius 1000 mm with its equatorial plane coinciding with the equatorial plane of the Rowland cylinder.

The inclusion of the entrance slit is facilitated by defining a screen (SCREEN 1) associated with Optical Element 1. A screen could be included anywhere in the optical system, either to interact with the beam (filter, slit etc.) or to facilitate examination of the beam. SCREEN 1 was defined as follows:

```
SCREEN 1

-------------------------------------------------------------------------

Position relative
to mirror:                    Before
Distance from mirror:         139.51
Aperturing:                   Yes
Open slit/solid stop:         Slit
Shape:                        Rectangular
Slit width/X-axis:            15
Slit height/Z-axis:           0.02
Absorption:                   No
```

Thus both the source and the optical system had been defined. On exiting from TRACE, the data from each optical element were separately stored in parameter files called START.01, START.02 etc. The parameter files were used to carry out the ray-tracing procedures, during the course of which binary output files were generated. These described the intercepts of the beam with either element surfaces (MIRR.01, 02 etc.) image/continuation planes (STAR.01, 02 etc.) or screens (SCREEN.01, 02 etc.).

A verbose explanation of all the methods and data employed to model the system is not included due to the amount of experimentation required to perfect the model. Only the results of modelling the optical system are given.

Shadow provided a set of programs to analyse the results of calculations. This work involved only PLOTXY, a utility which generated plots from the binary output files and PREPLOT, a utility which translated the unformatted binary files into formatted two column text files. The text files were exported (using the Kermit terminal emulation system) to an Apple Macintosh™ for plotting and analysis using Kaleidagraph™.

2.5.3 Ray-tracing results

Taking the plasma to be positioned approximately 60 mm [1] from the entrance slit (of 20 μm width), with an emitting region of diameter 0.25 mm (see section 3.5.2), the principal characteristics of the optical system were as follows.

Most of the diverging source beam was blocked by the slit, the spectrograph only collecting a small fraction (0.0007 %) of the total flux emitted[9] by the probe plasma. This allowed only a narrow portion along the centre of the grating to be illuminated, with approximately 35 % of the light from the slit missing the ruled area of the grating altogether. Thus the grating was fully illuminated along the l direction but only partially illuminated along the w direction. The illuminated width was found to be approximately 8 mm compared to an optimum width of approximately 22 mm (see section 3.1), thus the aperture of the system was found to be underfilled by a factor of 2.75.

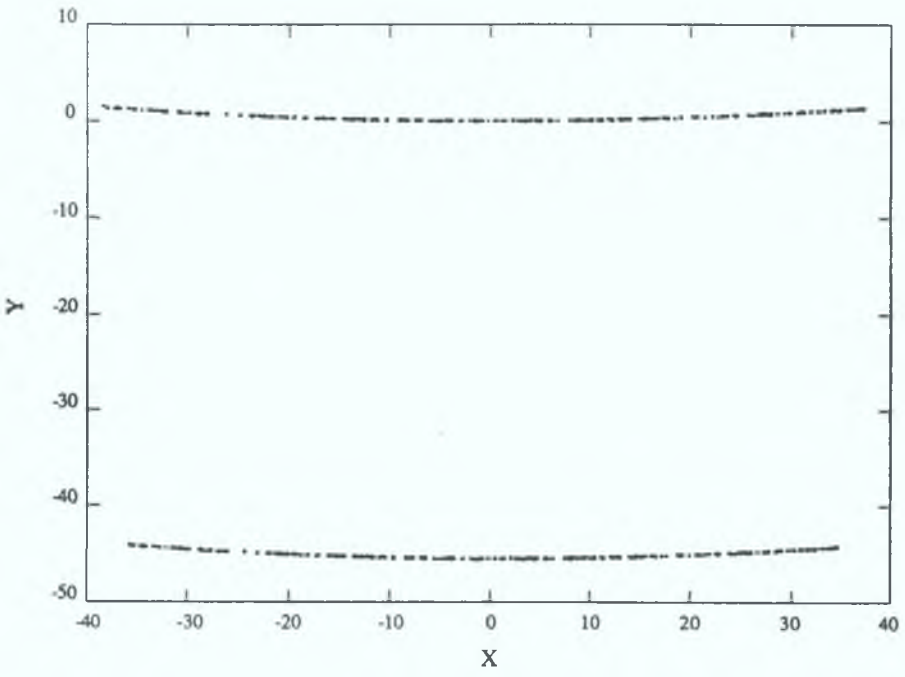

Figure 2.5. Ray-traced astigmatic spectrum featuring lines at 16.8 nm (centred on the origin) and 13.0 nm.

The monochromatic images formed at the Rowland circle had the form of long spectral lines, curved symmetrically about the circle. A ray-traced astigmatic spectrum with lines at 16.8 and 13.0 nm respectively is shown in figure 2.5, the Rowland circle lies in the equatorial or uw plane (the y axis ($x = 0$) in figure 2.5). The axes are scaled in millimetres with the

[9] Assuming that the plasma radiates uniformly into 4π steradians.

points $x = 0$ and $y = 0$ representing the plane of the Rowland circle and the position at which the 16 8 nm line is positioned on that circle, respectively (this format also applies to ray-traced images shown in subsequent chapters) The lengths of these astigmatic spectral lines were measured to be 65 mm at 13 0 nm and 75 mm at 16 8 nm Due to the fact that the SWR plates were only 51 mm wide with a useable width of only 38 5 mm (the remainder being covered by the plateholder), comparison of these values with plate observations were not possible However, comparison of the curvature of the ray-traced image to that of the experimental result was made Having located a plate which had been fully exposed to the long spectral lines, the curvature was estimated by assuming that the lines were sections of a circle and estimating their radius (this is not strictly true [4] but can be assumed for comparative purposes) The experimental radius was found to be 420 mm at 17 5 nm which compares reasonably well to a ray-traced radius of 515 mm at 16 8 nm The discrepancy of about 23 % being attributable to inaccuracies in the modelling process This result indicates that the ray-traced spectrum shown in figure 2 5 approximates what would be observed if the plates were sufficiently wide

2 5.4 Concluding remarks

Thus the optical system and the tools used to characterise it have been described The reasoning behind the modifications to the optics, developed in theory in chapter one and described in practise in the following chapters, are clear from section 2 5.3 above. Collecting such a small percentage of the flux emitted by the plasma was not such a problem on its own, indeed, only light from the probe that had passed through the absorbing plasma could contribute to an absorption spectrum When its effects were compounded by underfilling of the grating and spreading of the light across the long spectral lines observed at the Rowland circle, it was clearly a problem demanding attention.

References

1 Brilly, J , Ph D thesis, Dublin City University (1990) (unpublished)
2 Evans, D , private communication (1991)
3. Lai, B. and Cerrina, F, Nucl Instr & Meth , A246, 337 (1986)
4. Beutler, H G , J Opt Soc Am , 35, 311 (1945)

Chapter 3

The spatially resolved dual laser-plasma experiment

This chapter contains details of the modifications made to the system described in chapter 2 using the design concepts developed in chapter 1. The process by which the mirror parameters are assigned values is first discussed, then the design and construction of housing to incorporate the mirror into the system is dealt with. The procedure for aligning the optical elements with respect to each other is described in some detail, both for *ab initio* assembly of the system and routine alignment checking. The experimental procedure is then detailed and the chapter is concluded by a characterisation of the optical system using ray-tracing.

3.1 Toroidal mirror design

Design of the mirror was carried out in accordance with the conditions set down in sections 1.3.1 and 1.3.2. The system parameters required to perform the necessary calculations were the following:

$\lambda = 16.8$ nm	wavelength chosen to be stigmatic
$\alpha = 86.00°$	angle of incidence on grating
$\beta = 77.797°$	angle of diffraction (see equation (1.12))
$R_g = 2000$ mm	radius of curvature of grating[10]
$d_{sg} = 139.51$ mm	slit-grating distance ($d_{sg} = R \cos \alpha$)
$r_v = -449.47$ mm	virtual source distance (see equation (1.28))
$W_{opt} = 21.89$ mm	grating optimum width (see equation (1.29))

3.1.1 Angle of incidence

As outlined in the introduction, grazing incidence was required due to the low levels of reflectivity which result from the interaction of matter and XUV radiation. The physics of this interaction is generally described in terms of refractive index, n, which is a function of

[10] The subscript "g" was added to distinguish between grating radius and mirror major radius.

wavelength and the elements comprising the material reflecting the x-rays. In general the refractive index is slightly less than 1 and is complex, producing total external reflection. The critical angle, below which total external reflection occurs is calculated using Snell's law, which, for media of indices n_1 and n_2, is given by $\cos \theta_c = n_2/n_1$ where complex refractive index can be written as $n = 1 - \delta - i\beta$. Reflectivity curves for a given material are calculable by means of the Fresnel equations, which give the reflected amplitude at the boundary of two materials. δ and β, which characterise the scattering and absorbing aspects, respectively, of the matter-radiation interaction, are given by

$$\delta = k \rho f_1 / E A \qquad \text{and} \qquad \beta = k \rho f_2 / E A.$$

f_1 and f_2 are the real and imaginary parts of the atomic scattering factor, respectively, E is the photon energy, A is the atomic mass and k is a constant (with photon energy in eV and density in $g.cm^{-3}$, k = 415.22 [1]) The dependence of refractive index on the density, ρ, of the reflecting surface, as given by the expressions for the components of complex refractive index, necessitates the use of a highly dense substance, usually gold.

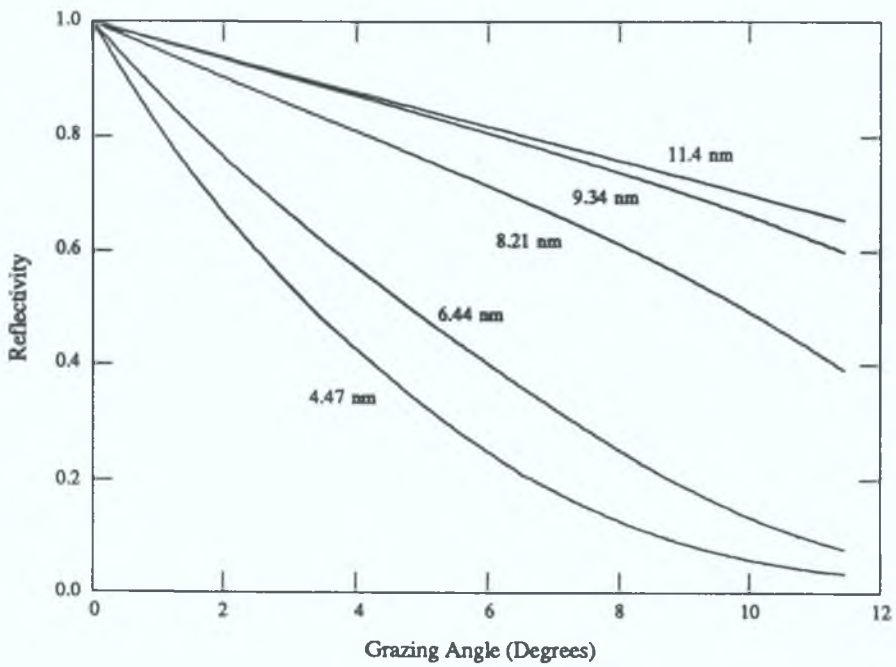

Figure 3.1. Reflectivity curves for gold as a function of grazing angle.

Incorporating the complex refractive index into Fresnel's equations [2] facilitates calculation of reflectivity curves as shown in figure 3.1. Such theoretical calculations cannot

account for such factors as surface roughness so it must be assumed that a precision-ground optical surface approximates an ideal one The f values for the wavelengths used were taken from low-energy x-ray interaction coefficient tables [3]

Taking 5 nm as the shortest wavelength to be of interest, it was concluded by inspection of figure 3 1 that a grazing angle of 4° was the most suitable (*i e* an incidence angle of 86°), producing about 50 % reflectivity (at 5 nm) A smaller angle, while increasing reflectivity, would reduce the effective area of the mirror and possibly introduce shadowing effects caused by the curvature of the mirror and a larger angle, while facilitating use of a smaller mirror, (see equation 1 30), would considerably reduce reflectivity at shorter wavelengths, *e g* a grazing angle of 8° (an incidence angle of 82°) would produce about 15 % reflectivity at 5 nm (see figure 3 1)

3.1.2 Source, primary image and secondary image distances

Shadow, the ray-tracing package, was not available at the time the toroidal mirror was designed so full optimisation of the design parameters was not carried out by ray-tracing

To eliminate the possibility of material emanating from the plasma contaminating the mirror, a suitably large value of r was chosen

$$r = 450 \text{ mm}$$

To avoid the requirement for an overly wide mirror (see equation 1 30) and the occurrence of an overly wide primary image (see section 1 2 4), the value of r'_1 was kept close to d_{sg}

$$r'_1 = 150 \text{ mm}$$

r'_2 was determined by adding the distances from the mirror to the virtual source (see figure 1.7), *i e* $r'_1 + d_{sg} + r_v$

$$r'_2 = 739 \text{ mm}$$

The radii required to meet the above specifications were calculated using equations (1 25) and (1 27)

Major radius, $R = 3225$ mm

Minor radius, $\rho = 39$ mm

3 1.3 Mirror width

The mirror width along the direction of the major radius (uw plane) required to ensure optimum grating illumination was calculated from equation (1.30)

$$w_{uw} = 24 \text{ mm}$$

3.2 Housing design and construction

The modifications made to include the toroidal mirror in the system were based on an existing system at the U S National Bureau of Standards, Centre for Radiation Research, Gaithersburg, Maryland, designed by T B Lucatorto and his collaborators [4] The target chamber described in chapter 2 was replaced by front-end optics consisting of a pair of horizontally aligned hollow cubes mounted on a levelled table The probe and absorbing plasmas were generated in one cube, the radiation from which passes through a pipe onto the mirror which was mounted in the second cube The spectrograph was mounted at an angle on a second table such that the radiation reflected by the mirror was directed along the spectrograph axis, as defined by a HeNe laser mounted on the target chamber The cube system and ancillary equipment are now described in detail

3.2.1 The target chamber

The target chamber consisted of a cube of aluminium of side length 127 mm through which three mutually orthogonal holes, of diameter 71 mm, were machined normal to each pair of adjacent faces respectively Four M4 tapped holes, on all except the upper face, facilitated attachment of the various flanges All components were machined from aluminium for ease of manufacture unless welding was required, in which case stainless steel was used

The bottom of the cube was supported by a stainless steel cylindrical column of flange diameter 127 mm and body diameter 97 mm The column was bored out to an internal diameter of 71 mm, with the hole emerging through the side of the column via a standard vacuum flange (63 mm internal diameter) welded onto the column. This facilitated connection to the vacuum system. Welded to the sides of the 63 mm flange were two 25 mm vacuum ports for connecting pressure gauges The column was bolted to a 10 mm steel plate supported by a welded 50 mm mild steel box-section table

The focusing optics for the lasers were mounted on an aluminium plate clamped around the column The two lenses were held by spring-loaded G-clamps mounted on three mutually orthogonal translation stages for controlling the position and focusing conditions of plasma formation The laser pulses were admitted to the target chamber by means of a 6 mm thick glass window secured to the front of the chamber by a circular aluminium frame of diameter 127 mm The effective window diameter matched the chamber bore of 71 mm

A similar window on the right-hand side of the chamber had an aluminium laser-cradle mounted over it The cradle featured screws to adjust the direction of the beam during alignment

The absorbing plasma was generated on the front face of a disc which is secured to the end of a sliding shaft by adhesive It was positioned by the sliding shaft (having two degrees of freedom, translation and rotation) attached by means of a Wilson seal to a flange bolted onto

the back of the chamber Target translation was quantified by spring-loading the protruding end of the shaft against a micrometer Rotation of the shaft facilitated supplying a fresh surface for repeated plasma production

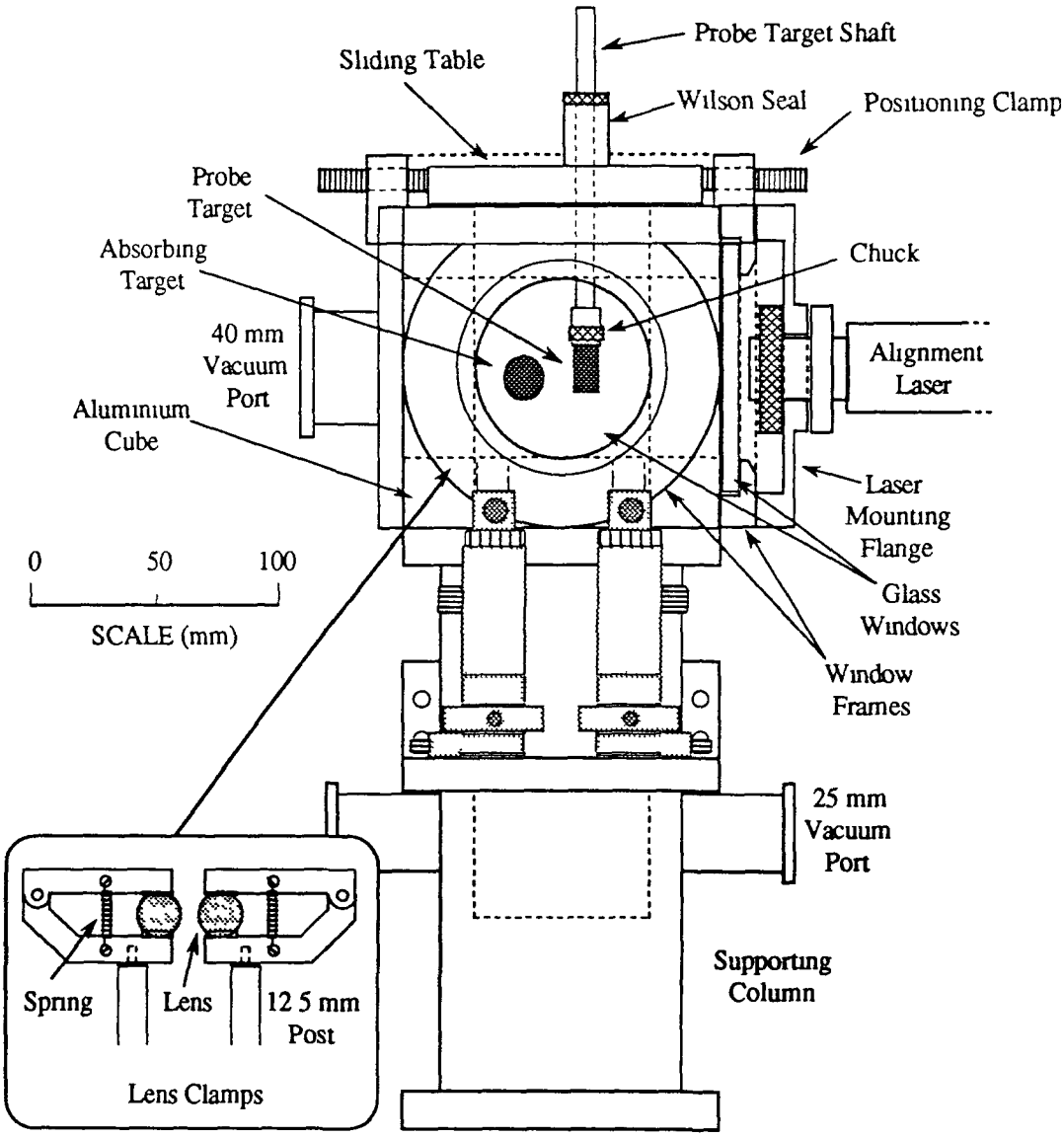

Figure 3 2 Front view of the target chamber showing side window in cross section and lens clamps displaced for clarity

The probe plasma was generated on the side of a cylindrical target which was secured to the end of a rotating shaft by a chuck The shaft was attached to a square table (of side 110 mm) by means of a Wilson seal The table rested (unbolted) on the top surface of the chamber such that it could slide across the chamber surface This allowed the target position to be controlled by a clamp around the top of the chamber, the motion being monitored by two micrometers, one for each degree of freedom Part of the shaft was threaded so that rotation produced helical motion of the target surface about its axis, supplying a fresh surface for

repeated plasma production.

Bolted to the left-hand face of the chamber was a stainless steel flange with a standard vacuum port (40 mm internal diameter) welded on to it. This was connected to the mirror chamber via an isolating valve and a length of stainless steel pipe. Figures 3.2 and 3.3 show front and side views, respectively, of the target chamber.

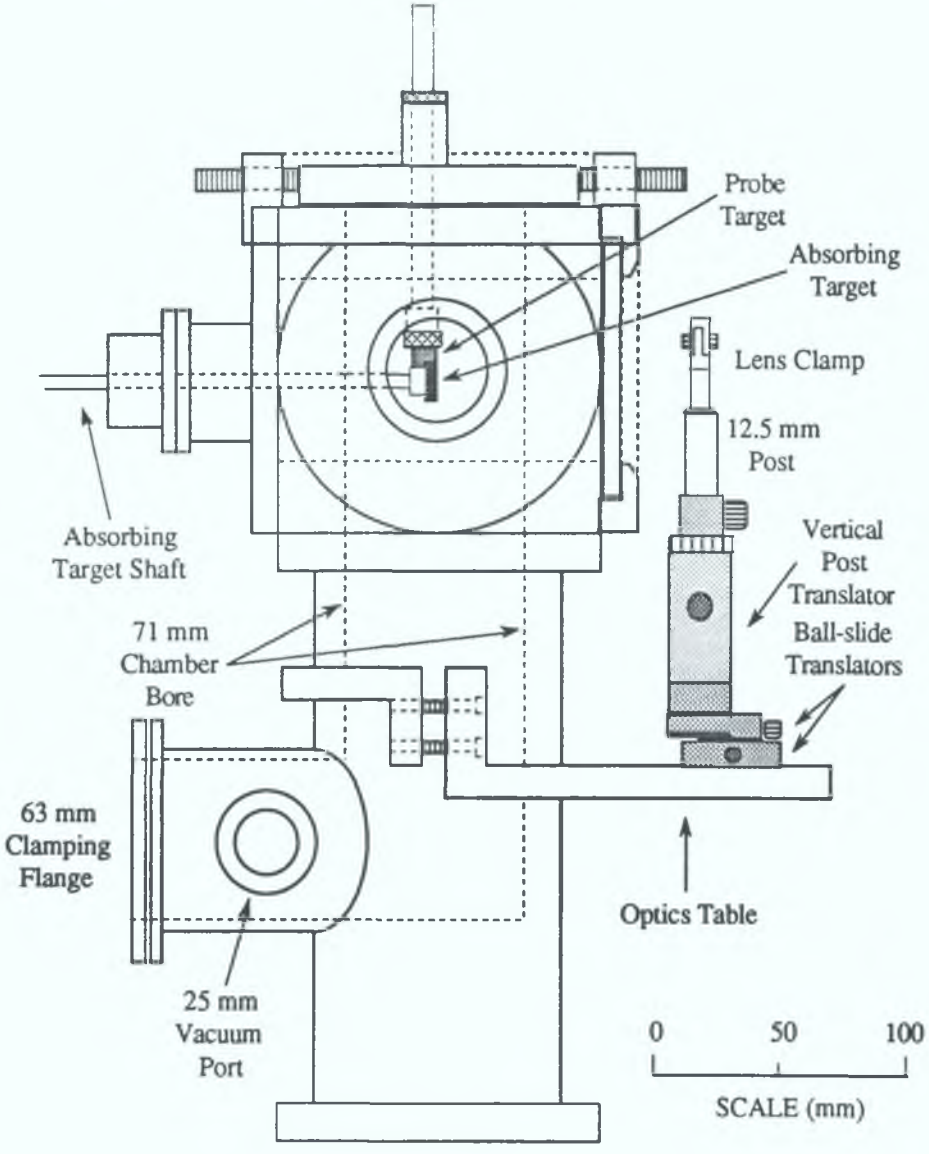

Figure 3.3. Side view of the target chamber.

3.2.2 The mirror chamber

The mirror chamber was identical to the target chamber except that all six faces were drilled and tapped with four M4 holes. The supporting column was also of the same design as that supporting the target chamber except that it was solid aluminium, having no connection to the vacuum system. It was bolted to the table as before.

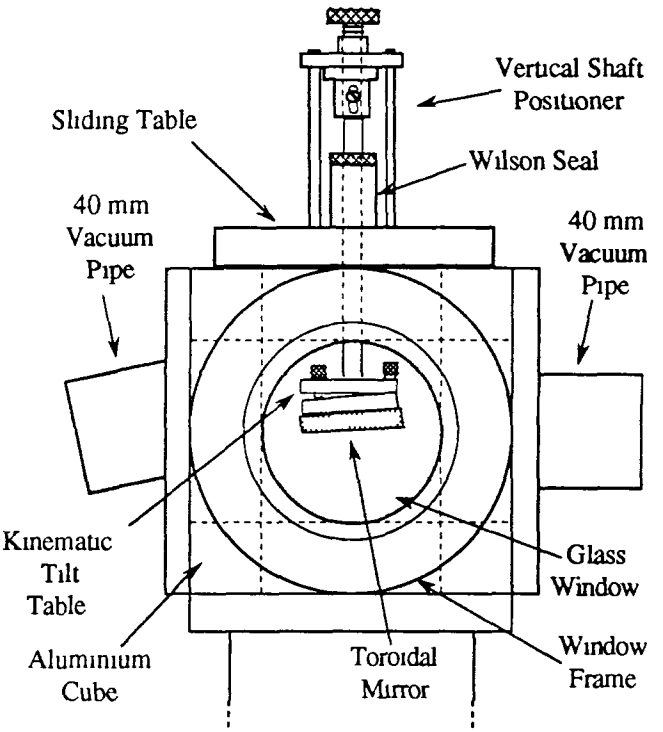

Figure 3 4. Front view of the mirror chamber

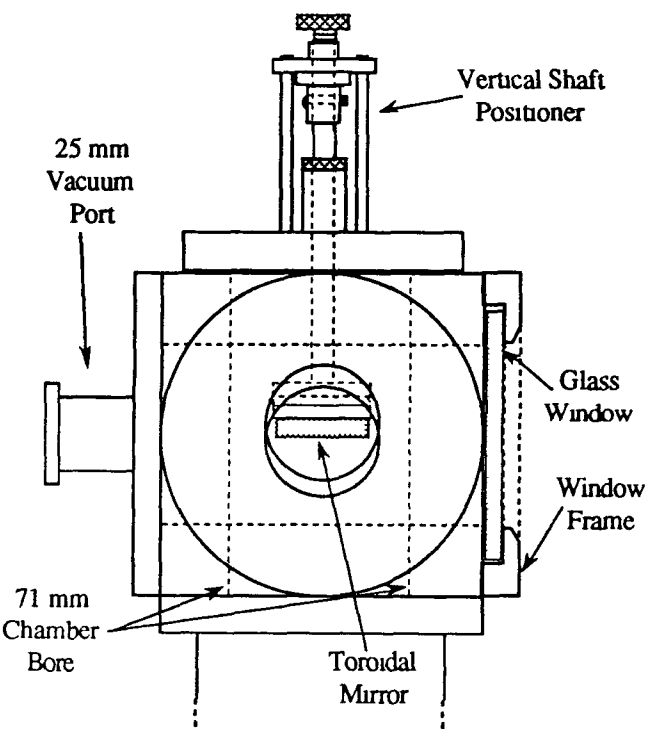

Figure 3.5. Side view of the mirror chamber

Bolted to the left- and right-hand faces of the cube were stainless steel flanges with attached vacuum ports (40 mm internal diameter). The right-hand port was connected to the pipe from the target chamber, the left-hand port was mounted at an angle for connection to the slit-housing flange by means of a short rubber hose. The hose served to decouple the front-end table from the spectrograph table.

The back of the chamber was connected to the spectrograph tank via a 25 mm port and a flexible steel pipe to equalise the chamber pressures on either side of the slit.

The toroidal mirror was clamped by lightly sprung aluminium jaws onto a kinematic tilt table for precise angular adjustment. The table (model 14004, supplied by Oriel) featured fine pitch screw adjustment with an angular range of ±4°. It was screwed onto the end of a 14 mm diameter shaft which was attached to a square table via a Wilson seal in a similar manner to the probe target holder except that rotation of the shaft was not permitted, only vertical translation by means of a finely threaded positioner at the top of the shaft. The table was bolted to the top face of the chamber by M4 bolts through oversized clearance holes (8 mm) allowing ±2 mm adjustment of table position (for alignment purposes) on loosening the bolts.

The front face of the cube was covered by a window identical to those on the target chamber. Access to the tilt table adjustment screws was gained by removing the window. Figures 3.4 and 3.5 show front and side views, respectively, of the mirror chamber.

3.2.3 The focusing optics and lasers

The mounting plate for the lens holders had a usable length of 70 mm and was 127 mm wide. Each (circular) lens was held by a custom designed spring-loaded G-clamp with a curve-matched lower jaw. The clamp was attached to a standard 12.7 mm post which sat in a vertical post translator (model M-VPT-3, supplied by Newport) with a range of ±6 mm, giving precise control over the vertical position of the lens. The post holder was mounted on a horizontally stacked pair of mutually orthogonal ball-slide translators (model M-450A, supplied by Newport) with a range of ±3 mm, giving precise control with two degrees of freedom in the horizontal plane. Figures 3.2 and 3.3 include front and side elevations of the lens mount.

The lasers were positioned with the YAG aimed directly at the probe target and the ruby at 90° to the YAG with a beam-steering mirror mounted such that the ruby beam was deflected along a path parallel to the YAG beam in the direction of the absorbing target. This is necessitated by the short distance between the two targets (10 - 30 mm).

3.2.4 The vacuum system

The spectrograph side of the system was pumped (as described in section 2.1.1) by a turbomolecular/two-stage rotary pump combination, with the turbo mounted below the grating housing and the rotary housed under the spectrograph table, the two being connected by a

corrugated stainless steel pipe of 40 mm internal diameter The purpose of the corrugations was for flexibility and to decouple the vibrating rotary pump from the rest of the system

To compensate for the increased volume and more complex internal shape of the modified system, the target chamber was connected to a Diffstak® diffusion pump (supplied by Edwards High Vacuum) which was backed by a two-stage rotary pump The Diffstak was connected to the target chamber's supporting column by a 63 mm diameter corrugated pipe which passed through a hole in the front-end table, the pumping rig being housed under the table

Using both pumping systems together, roughing[11] from the spectrograph side and then opening the Diffstak, facilitated pumping down to a working pressure of about 10^{-2} - 10^{-3} Pa in less than fifteen minutes, assuming that the system was being used regularly

All connections and flanges were sealed by nitrile rubber O-rings which were lightly smeared with vacuum grease to prevent degradation of the rubber under repeated compression and expansion cycles as the system was evacuated and vented

A manual gate valve was included between the target chamber and mirror chamber so that the two sides of the system could be evacuated or vented separately This allowed a plate to be changed without disturbing the target chamber or a target to be changed without having to vent the mirror chamber and spectrograph tank, thus reducing the turnaround time of experiments

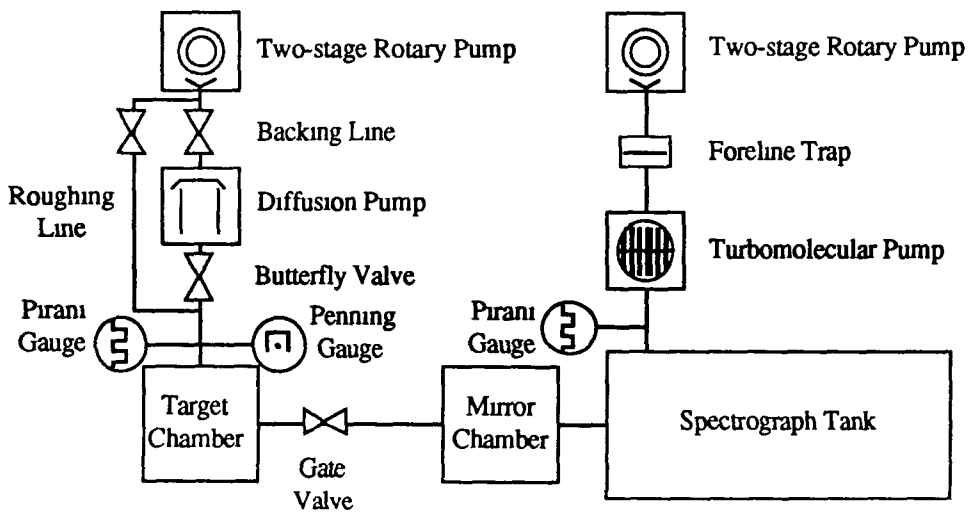

Figure 3.6. Schematic of the vacuum system

Pressure was measured at two locations at the flange connecting the turbo pump to the spectrograph and at the flange connecting the Diffstak to the target chamber Most of the pumping process was monitored using a Pirani gauge, a device that works on the principle that the thermal conductivity of a gas is proportional to pressure, which has a range from 10^{2} down to about 10^{-1} Pa, becoming somewhat inaccurate close to its lower limit When the Diffstak was in operation, this limit was quickly reached necessitating the use of a Penning gauge, a

[11] The initial pumping stage using the rotary pump to reduce chamber pressure to about 10 Pa.

high voltage device that works on the principle that discharge current has a dependency on pressure at fixed voltage This has a range from 10^{1} down to 10^{-5} Pa thus being ideal for monitoring the vacuum when at working pressures One Penning gauge was included between the target chamber and the Diffstak A schematic diagram[12] of the system is shown above (see figure 3 4)

3.3 Alignment

The addition of an auxiliary optical element to compensate for astigmatism in the concave grating meant that there were five independently adjustable optical elements Fortunately, three of these could be treated as one, assuming that the slit, grating and plate holder were correctly aligned in the spectrograph Thus the spectrograph must be aligned to the toroidal mirror and the source, the mirror being the critical element as the source position was treated as an experimental variable The alignment process is described below as a three stage procedure, from commissioning the system to experimental alignment

3.3.1 Initial alignment

Commissioning the system obviously required that a complete alignment process be developed to correctly position the optical elements This process proved to be tedious to perform unaided, so several tools were designed to simplify the process The steps involved are now described.

1. Defining the optic axis (from source to mirror):- The two cubes were positioned such that they are accurately aligned with respect to each other, thus defining a frame of reference The optic axis was defined as the line joining the cube centres, and the alignment laser (HeNe 1) was positioned to the right of the target chamber with the beam centred on the optic axis (see figure 3.7). The process of aligning the HeNe was facilitated by two templates which, when positioned carefully on the upper faces of the mirror and target chambers respectively, had narrow apertures (approximately 1 mm) defining the optic axis

2 Defining the optic axis (from mirror to detector) - To define the optic axis after the mirror (without placing the mirror in its correct position), required the temporary introduction of a second HeNe (HeNe 2) This was mounted directly above HeNe 1 (in the same vertical plane) with its beam directed downward at an angle of 8° (twice the angle of incidence on the mirror) to that of HeNe 1 such that the two beams intersect at the centre of the mirror chamber. To assist in finding the correct intersection point, the mirror chamber template featured two apertures, one defining the horizontal pre-mirror axis and another at 8° to the horizontal, with

[12] ISO Standard Graphic Symbols [5] are used

the two crossing at the cube centre. As the path of HeNe 2 was blocked by the target chamber, the latter was removed before finalising the position of the former. The correctly positioned beam of HeNe 2 defined the optic axis to which the spectrograph must be aligned.

3. Aligning the spectrograph to the optic axis:- The spectrograph was mounted at an angle of 12° to the horizontal on its table (the angle of incidence on the grating added to 8°). The table was moved into position such that the slit was 150 mm from the centre of the mirror chamber and was centred on the beam of HeNe 2. To simplify accurate positioning of the spectrograph, the axis was chosen to pass through an access hole at the back of the tank (unfortunately the axis did not pass precisely along the meridional plane of the Rowland circle but this is of little consequence as spectral quality is not affected). Using a plug-template placed in the access hole and adjusting the table position until the laser speckle pattern covered the spot on the plug, the correct spectrograph position was found. To fine-tune this position, both central incidence of HeNe 2 on the grating and quasi-central intersection of HeNe 2 with the zero order image location on the Rowland circle were checked.

4. Replacing the target chamber (removed at Step 2 above):- A further laser, HeNe 3, was placed such that it followed exactly the path of HeNe 2, except that it entered from the back of the spectrograph. This facilitated removal of HeNe 2 from the system and thus the target chamber was replaced and HeNe 1 mounted on it (as shown in figure 3.2).

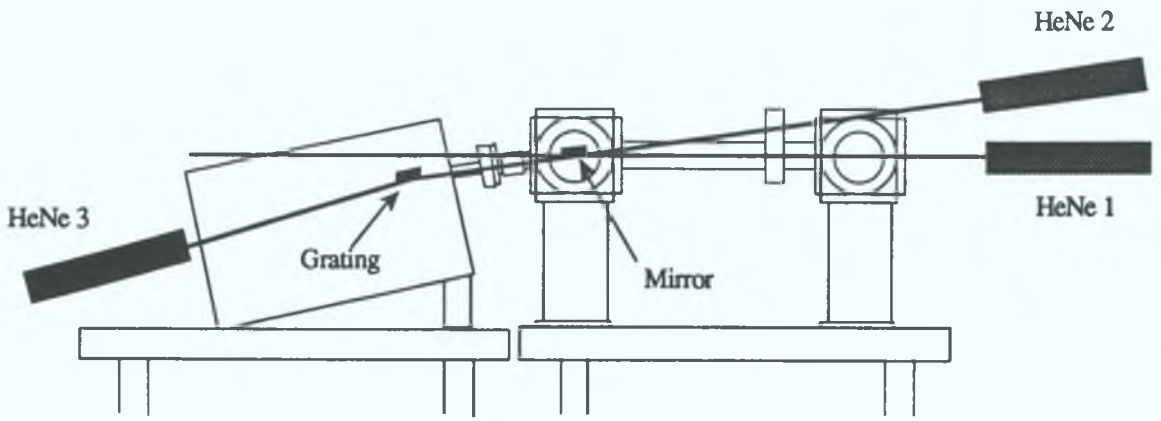

Figure 3.7. Schematic of the alignment setup.

5. Positioning the toroidal mirror:- The correct mirror position was found by placing it such that it was aligned with the major radius parallel to the optic axis and its pole at the point of intersection of the two beams. The angle of the tilt table was then adjusted until the beam paths were exactly coincident. Due to the fact that the mirror was mounted via an O-ring-sealed table on the cube, the cube was evacuated to working pressure and the mirror table secured by hand-tightening its four bolts with the O-ring in its compressed state. The cube was then vented and the vertical position of the mirror adjusted to account for the O-ring compression. This ensured that the mirror would not move on repeated pumping and venting of the system.

6. Checking the alignment:- To check that the system was properly aligned, a pinhole was placed at the source position to simulate a point source. The primary and secondary

images (the primary image should be a curve, centred on and symmetrical about the slit centre) were inspected, as were the illuminated spots on the mirror, grating, zero order image location and plug template. At this stage the back-projected laser, HeNe 3, was removed.

On initial assembly of the system, the above procedure was applied to correctly align the optical elements. The templates were designed during the alignment, principally for the benefit of those who may repeat the process after over-hauling or moving the system. The slit was opened to a width of approximately 100 μm to allow a sufficient light flux through the system, this avoided having to work in low light conditions during alignment.

3.3.2 Operational alignment

Reliability testing carried out after alignment showed that the assembled system was susceptible to vibration and general disturbances which caused it to drift out of alignment over a period of time. Preventative measures to minimise this drift included: removing all excess equipment from the tables to minimise user contact with the apparatus; exercising care with all remaining contact (no leaning on the tables etc.); regularly using the apparatus and checking that it is correctly aligned before running experiments. To simplify checking the alignment, the sliding mask between the grating and plateholder (see section 2.1.1) was modified to hold a photodiode mounted such that it could be scanned across the optic axis. Thus the intensity profile of the beam could be recorded in terms of a plot of voltage against distance. The circuit used to measure the relative intensity of the beam is shown in figure 3.8.

The method devised for routinely checking the alignment and keeping written records was a two part process. The first part involved using the alignment laser to determine whether or not the system had been disturbed since the last experiment or set of experiments. This process need not be repeated each day or for each experiment, but with a frequency which depended on the user's familiarity with the equipment. The second part involved optimising the position of the plasma in the target chamber (experimental alignment) using the photodiode. By comparison with previous results on a day to day basis, the experienced user could spot the onset of performance degradation, and thus would not need to check using the HeNe laser. As the experimental alignment should be carried out immediately before running an experiment, it is dealt with in the next section (section 3.4). The HeNe-based alignment check consisted of the following steps.

1. Inspecting the alignment of optical elements to the axis at atmospheric pressure:- The target chamber and slit housing were stripped down. The target template was placed on the target chamber and the centre of the beam was checked to ensure that it passed through the aperture and was centrally incident on the mirror. The image was inspected to check that it was centred on and symmetrical about the slit. The plug-template was inspected to check that the laser spot was correctly incident at the back of the spectrograph tank.

2. Checking the relative intensity profile of the HeNe beam at working pressure:- The

system was prepared for experiment and evacuated (see section 3.4.1). Using the micrometer head, the photodiode was scanned across the laser beam, noting the output voltage (measured using an oscilloscope or voltmeter) on every half millimetre increment. Voltage was plotted against position. The diode was placed at the position of maximum voltage and the vertical position of the mirror was adjusted until the voltage reached a maximum.

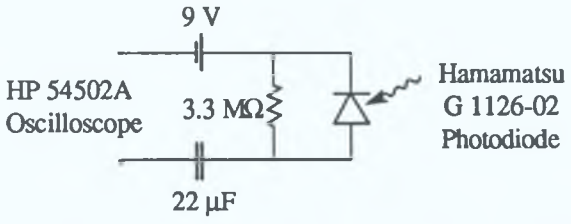

Figure 3.8. Diagram of photodiode detector circuit. The quartz window on the photodiode was removed to facilitate XUV sensitivity.

These guidelines were designed to provide a framework for relatively trouble free operation of the system. If sufficient care were not taken at all times, the need for realignment of one or more optical elements could result.

3.4 The experimental procedure

Having set up the apparatus as described in section 3.3 above, the procedures used to photographically record an XUV spectrum are now given.

3.4.1 Experimental preparation

The preliminaries required to prepare the apparatus for recording a spectrum, with the exception of fine tuning the alignment, were as follows.

1. For the experiments described here, the probe plasma was generated on a tubular tantalum (Ta) target mounted in a chuck as described in section 3.2.1. The target for the absorbing plasma is generally prepared and mounted for each experiment. Different metals present different handling/mounting problems to the experimentalist. This work involved only aluminium absorption, so these problems are not discussed. The aluminium target was prepared by machining the sample to the required dimensions and attaching it to the target holder using a cyanoacrylate adhesive. The targets were positioned such that when the lenses were set up and the lasers aligned (YAG to probe target and ruby to absorbing target), the plasma positions were approximately on the optic axis (as defined by the alignment HeNe).

2. A photographic plate was loaded into the spectrograph (see section 2.1.2, step 2).

3. The system was evacuated as follows. The Diffstak oil-heater was switched on, having first checked that the butterfly valve was closed and the backing line was operational (see figure 3.6). All fittings/flanges were checked and tightened or secured if necessary. The turbomolecular/rotary combination was started, having checked that the target chamber isolation valve was open. The whole system was pumped by the turbomolecular/rotary combination until the pressure reached 1 - 5 Pa, at which point the Diffstak butterfly valve was opened, rapidly bringing the system down to working pressures (10^{-2} Pa). It should be noted here that if the operational alignment procedures were being applied, then step 2 of section 3.3.2 would be implemented at this stage.

4. The required inter-plasma time-delay was selected using the synchronisation electronics as described in section 2.1.2, step 4.

3.4.2 Experimental alignment

This procedure was carried out principally to correctly position the plasmas in the target chamber, but, as mentioned in section 3.3.2, also served to routinely produce relative intensity profiles of the XUV beam between the grating and detector using the photodiode. The inclusion of micrometers allowed the experimentalist to quantify the probe target location in terms of x and y coordinates, however, reference to specific coordinate values is avoided due to their dependence on how the target was fitted. Experimental alignment of the probe target involved the following steps.

1. The spectrograph photodiode was set up as in figure 3.8, with the oscilloscope operating in storage mode, triggered by the Q-switch synchronisation pulse of the YAG. The oscilloscope settings were: timebase = 500 μs; resolution = 1.5 V/cm; delay = 0 s; input impedance = 1 MΩ.

2. Using the micrometer head, the photodiode was scanned across the axis, firing the laser and noting the maximum voltage (if a pulse was observed) on each half millimetre increment. From this data, the maximum pulse height and the position at which it occurred were noted.

3. The target was moved horizontally toward or away from the mirror by 0.5 - 1 mm using the micrometer head provided (see section 3.2.1). Step 2 was repeated. If the new maximum pulse height was found to be greater than the previous one, then the target was moved again in the same direction and step 2 was repeated again. If not, then the target was moved in the opposite direction and step 2 repeated. This process was continued until the position of largest pulse height was found.

4. A repeat of step 3 except that the target movement was to 0.5 - 1 mm behind or in front of the approximate on-axis position, again using the micrometer provided. In this case, the position of largest pulse height should ideally be within 3 mm of the central position, if not, one of the optical elements (or the HeNe) is out of alignment.

5. Repeat of step 3 except that the lens was moved to 0 5 - 1 mm above or below the approximate on-axis position, using the vertical post translator (see figure 3 3) Again, the position of largest pulse height should ideally be within 2 - 3 mm of the central position

Either a plot of pulse height against position after optimisation or simply a record of the maximum pulse height achieved could be used to monitor the performance of the system from day to day Experimental alignment of the absorbing plasma relative to the probe plasma location was carried out as follows (assuming that the photodiode was left at the point of maximum pulse height)

1 The absorber was moved in toward the optic axis (using the micrometer) until it cut across the axis, blocking the beam path and thus reducing the observed pulse height to zero

2 The absorbing target was then retracted until the signal had just returned to its maximum level, at which point the beam-centre was said to be skimming the surface of the target It was then retracted by a further amount which depended upon the portion of the plasma to be probed (typically 0 1 - 3 0 mm)

3 The second vertical post translator (in front of the absorbing target) was adjusted to ensure that the two plasmas would be generated in the same horizontal plane, so that the probe beam would pass through the absorbing column

3.4.3 Exposing and developing the plate

The delay generators were reconnected to the lasers (having been disconnected for the optimisation), the shutter on the plateholder was opened and the required number of laser shots (usually 5 to 15) were fired, during which, a note of the time delay between the pulses of each shot were noted (so that electronic jitter could be ruled out as an error source). The plate had thus been exposed.

Automatic venting the system was initiated by closing the Diffstak butterfly valve and switching off the turbomolecular/rotary controller The venting process took a little over 5 minutes

Developing the plate involved removing it from the holder under safe light conditions, immersing in agitated developer (Kodak D-19 dissolved as directed and diluted 2 1 with water) for 2 minutes, rinsing in water and immersing in fixer (Kodak Unifix™ diluted 3 1 with water) for 7 minutes A further rinse ensured that the fixer was washed off and the developed plate was left to dry

Several experiments were carried out both to perfect the required techniques and to thoroughly test the apparatus The results of these experiments and the general performance of the system are discussed in chapter 4.

3.5 The optical system

The modified apparatus, *i e* the toroidal system, was characterised using Shadow, the ray-tracing package A description of Shadow and its operation is given in sections 2 5 1 and 2 5 2, so the following sections will describe only the data required to characterise the optics and the results obtained by modelling the system

3 5 1 Source modelling

Using a combination of a review of Shadow and its documentation and observations from plates, two models applicable to the plasma source were arrived at

An elliptical or circular source can be assigned dimensions such that it has similar spatial extent to the continuum emitting region of the laser plasma used in experiment. By trial and error methods (with an initial guess based on geometric calculations), measurements of continuum width on plates of 0 5 mm at 16 nm (see figure 4 1) were reproduced by ray-tracing using a circular source with a radius of 0 125 mm

To obtain information about the imaging characteristics of the system, a point source was used This allowed the contribution to the image from various parts and positions of the source to be examined.

The angular distribution of emission is of equal importance to the spatial characteristics of the source The plasma was considered to be a radiating gaseous sphere emitting with uniform brightness *i e* the flux flowing into a solid angle $d\Omega$ from an area dA is independent of the observation angle

Various values for the angular divergence of the source were employed in the ray-tracing procedures. In general, the smallest possible divergence was used to avoid loss of light, *e g* the source just filled the mirror in the case of the stigmatic experiment, the source divergence values for which were calculated using a cosine projection of the mirror dimensions through 86° to calculate its effective area. The source file for which was as follows.

```
SOURCE 2

-------------------------------------------------------------

File to store rays:     BEGIN2
Source type             Random
# rays                  5000
Spatial type:           Ellipse
      Width (X):              0 125
      Height (Y):             0.125
```

```
Depth.                    Off
Angle distribution        Uniform
      Divergences (in Radians)
      Horizontal  (X+)          2 668 E-2
                  (X-).         2 668 E-2
      Vertical    (Z+)          2 648 E-3
                  (Z-)          2 648 E-3
Photon energy dist        Single Line
      Units                     Ångstroms
      Photon energy             168
```

This is similar to Source 1 (section 2 5 2) with the exception that here the aperture was matched to that of the mirror and emission was restricted to a single wavelength Source 1 was applied to both optical systems for comparative reasons (see section 4 2) Some of the analytical work employed another source (Source 3), which was the same as above except that the spatial extent was reduced to a point.

3.5.2 System modelling

As before, the system parameters were entered from within the TRACE module of Shadow's command level The optical system was similar to that described in section 2.5.2 except that the toroidal mirror is inserted before the grating. Using the menu option for an exit slit on the extra optical element, the screen defined as SCREEN 1 was made redundant. The toroidal mirror was defined as follows.

```
OPTICAL ELEMENT 1

_____________________________________________________________

Source file name          BEGIN2
Source plane distance     450
Image plane distance:     150
Angle of incidence        86
Angle of reflection·      0
Type of element           Reflector
Figure·                   Toroidal
      Mirror parameters·
```

```
            Foci and continuation
            planes:              Coincident
            Toroidal mirror
            pole location:       Lower/outer
            Major radius:        3225
            Minor radius:        39
      Surface curvature:         Concave
      Limits check:
            Shape:               Rectangle
            Dimensions  X(+):    12
                        X(-):    12
                        Y(+):    17
                        Y(-):    17
Diffraction:                     Mirror
Exit slit:
      Length (sagittal):         15
      Width (tangential):        0.02
      Tilt (CCW):                0
```

Optical elements 2 and 3 represent the grating and photographic plate respectively, as given in section 2.5.2 as elements 1 and 2. As before, a verbose explanation of all the methods and data employed to model the system is not included, only the results of modelling the optical system are given.

3.5.3 Ray-tracing results

Reproduction of the continuum widths produced by a tantalum plasma provided the first indications of successful modelling. This and the other data produced clearly showed that the relatively simple modelling procedures applied resulted in an accurate description of the optical system. The main characteristics of the optical system were as follows.

Light from the source was collected by the toroidal mirror and focused onto the slit. The solid angle subtended by the mirror to the source was small because of the grazing incidence, the mirror thus collecting a small fraction (0.002 %[13]) of the total flux emitted by the probe plasma.

The (primary) image formed at the slit was found to be a small curved section 18 mm

[13] This figure has little real meaning as only the portion of the beam which passed through the absorbing plasma can contribute to an absorption spectrum.

in length and approximately 0.15 mm in width (see figure 3.9). Thus most of the light focused at the slit was lost with only about 4 mm of the slit length being utilised, admitting around 5 % of the light to the system for a slit width of 20 μm.

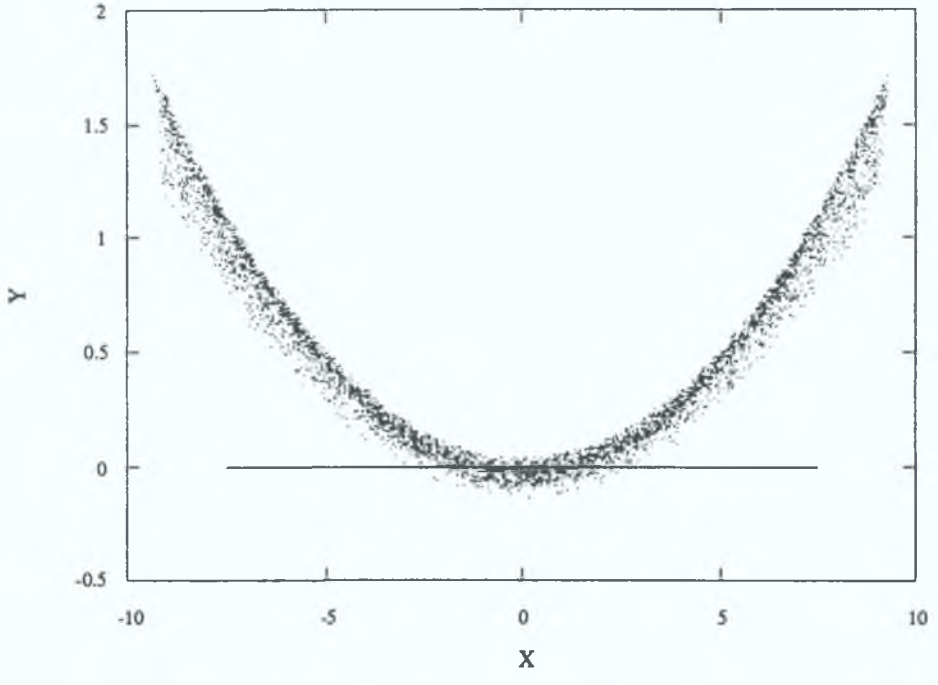

Figure 3.9. Ray-traced cross section of the beam at the slit (line denotes slit).

The beam was incident centrally on the grating, producing a blurred X-shaped footprint (see figure 3.10(a) and (b)), where the paired lobes represent stages between the separate horizontal and vertical foci of the mirror.

More detailed analysis showed that the primary image dimensions (length and width) were proportional to the dimensions of the illuminated portion of the mirror, in general agreement with theory as derived from T_3 of the optical path function (see equation (1.24), section 1.2.1 and equation (1.28), section 1.2.3). Thus the extension of the image in the x direction was found to be dependent on the extent of mirror illumination in the x direction and similarly for the y direction. For example, illuminating a narrow central portion of the mirror of dimensions 3.4 mm in x and 20 mm in y produced an image 2.5 mm in length and 0.09 mm in width. Almost 30 % of the rays forming this small image passed through the slit. The conclusion of this analysis was that due to the aberrations in the primary image, the effective (or utilised) area of the mirror was less than 10 % of its actual area. Fortunately, the main limitation on the aperture of the system caused by this was in the x *(l)* direction and so did not adversely affect resolution (*i.e.* the optimum width of the grating was filled (see figure 3.10 (b))), but did however reduce the flux admitted to the system.

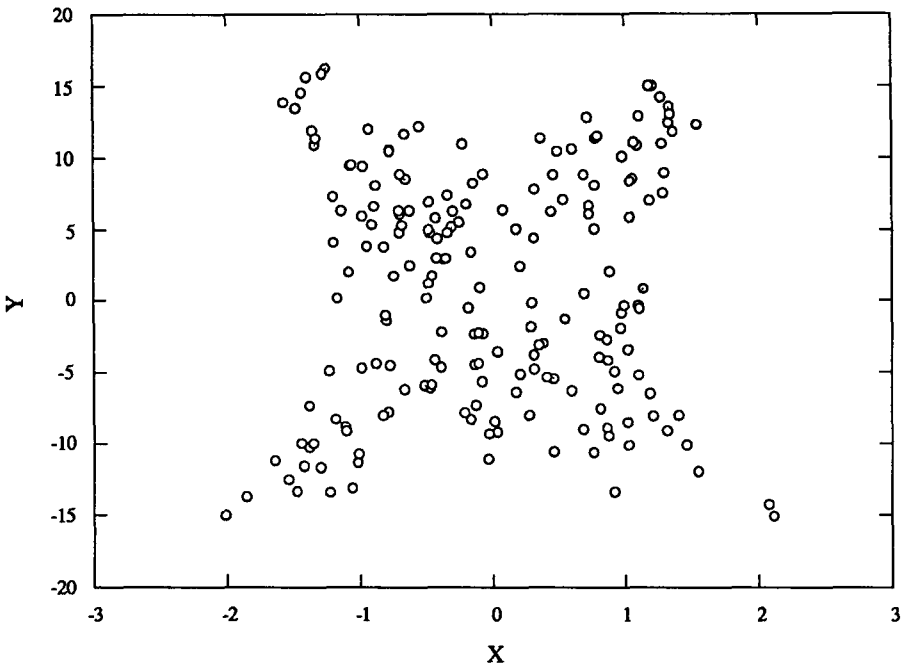

Figure 3.10 (a). Beam footprint on the grating (scaled axes)

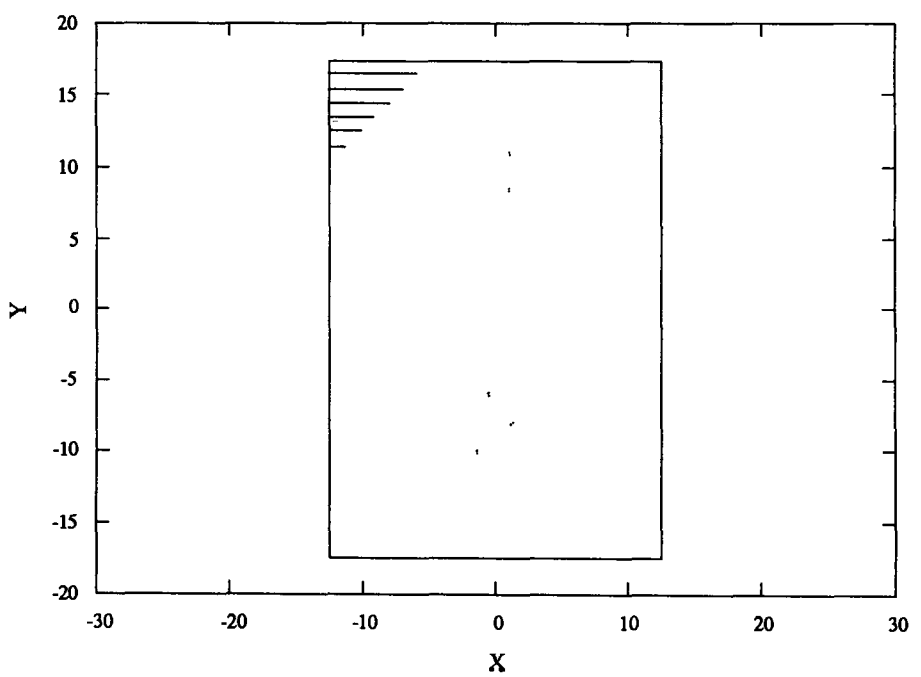

Figure 3.10 (b). Beam footprint (Cartesian axes with grating ruling indicated)

Due to the focused nature of the beam, all the light contributed to the image once admitted to the system via the entrance slit (ignoring reflection losses). The image produced at the Rowland circle is shown in figure 3.11 (b). The image (spectrum) shown, which consists of a single line at 16.8 nm, was produced by an ideal monochromatic source. Such a source was used for most of the analyses to concentrate the limited number of rays into one spectral region.

The line width (measured in the y direction) in this case was purely a result of grating focusing, providing a theoretical minimum value of the width, but neglecting the effect of the numerous line broadening processes which occur in real sources. The measured width of 0.09 mm was found to be equivalent to a spectral linewidth[14] of 0.008 nm. This compared to experimental observations [6] of what would be considered narrow lines having widths of about 0.01 nm. Linewidths of broadened spectral features could be up to 0.06 or 0.07 nm wide.

The line length (x axis) was measured to be approximately 0.5 mm. This was a result of the stigmatic image of the source being magnified by the optical system by approximately a factor of two. The magnification of the system was calculated by geometry (from the ratio of image distance to object distance) to be 1.64 at 16.8 nm, the discrepancy between the figures being accountable in terms of the various aberrations of the system. As in figure 3.11, the images were generally devoid of clearly defined edges, again due to the aberrations, so determining the dimensions of the image was a matter for some arbitration. This also applies to experimental measurements, particularly in the case of photographic instruments, which make computerised analysis difficult.

Having modelled the characteristics of the optical system operating in its simplest mode, *i.e.* producing a monochromatic image of a plasma source positioned on the optical axis which emitted at the stigmatic wavelength only, a more complete analysis is now required. In fact, by its own definition, the probe plasma emitted a continuum in the XUV. For a more complete description, the following two approaches were adopted.

1. To determine the ability of the system to image radiation at wavelengths other than the optimum, three more points were chosen, one at 5 nm below the optimum, one at 5 nm above and one at 5 nm above that again. Figure 3.11 shows the monochromatic images at the four wavelengths chosen, (*i.e.* 11.8 nm, 16.8 nm, 21.8 nm and 26.8 nm) produced by ray-tracing.

2. To determine the ability of the system to image sources not centred on the optic axis (or the ability to image sources of larger spatial extent that those considered thus far, such as laser plasmas produced on lighter elements, *i.e.* those of atomic number less than 73), images of a point source in several different locations were generated to represent individual elements of an extended source.

[14] Conversion to wavelength is facilitated by calculating the linear dispersion (0.088 nm/mm in this case) at the required position on the Rowland circle (see reference [2], chapter 1).

The main characteristics of the four wavelength samples, as used to characterise continuum emission by a 0 25 mm plasma, were as follows.

The image widths were all measured to be approximately 0 1 mm, indicating that the grating focusing (in the *uw* plane at least) is independent of position on the Rowland circle This is clearly in accordance with theory as the grating focus was earlier described in terms of the Rowland circle (see section 1 1).

Examination of the image lengths in figures 3 11 (which are subsequently referred to as (A), (B), (C) and (D) respectively, as m the diagram) lead to the analysis of them in terms of two main features measured image length (measured in the same way as a plate feature, *i e* the edge of the feature being placed by the observer where the image density or "plate blackening" falls to a sufficiently low level) and relative density of points along the image

Applying these criteria to the optimum wavelength of 16 8 nm (B), the nominal length of the image was measured at 0 5 mm with a fairly constant point density falling off rapidly at the edges The length of (A) was measured to be approximately 0 4 mm Its profile differed from (B) in that it had a higher point density toward the centre which fell off more slowly at the edges The length of (C) was found to be approximately 0 6 mm Its profile also differed from (B) in that it had a lower point density at the centre which also fell off more slowly at the edges The length of (D) was found to be of the order of 0 7 - 0 8 mm It had the lowest point density and exhibited the most gradual decay at the edges

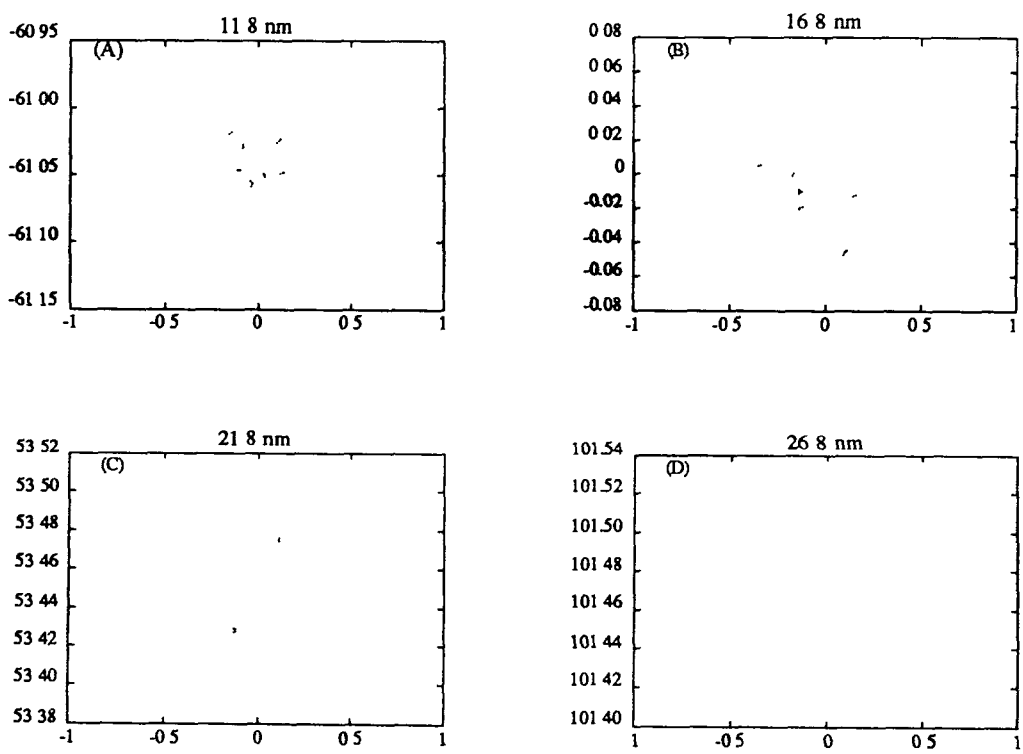

Figure 3.11. Ray-traced images at four sample wavelengths
(the axes are designated as in figure 3 10)

These features were readily explained by relating the two criteria of analysis to two aspects of the theoretical description Firstly, the measured image lengths could be accounted for in terms of the differing wavelengths having differing image distances and thus being images of the source magnified by differing amounts (from the ratio of image distance to object distance) As mentioned above, some numerical discrepancies existed but there was general agreement Secondly, the observed degradation of the image profile as the wavelength deviated from 16 8 nm in either direction on the Rowland circle was simply due to the fact that the virtual source supplied to the grating by the mirror only produced a focus in the *uw* plane at one point on the Rowland circle (see figure 1 8 (a)), thus, for all other points the image was out of focus by an amount proportional to its distance from the optimum wavelength

The final stage of the modelling process was to examine the effect of imaging off-axis source points This was carried out as follows

The analysis was restricted to a monochromatic source emitting at 16 8 nm to avoid the defocusing effects discussed above To further simplify the process, a point source was used The images that resulted from varying the source position from on the optic axis to 4 mm off axis (in increments of 1 mm) in the *wl* plane (see figure 1 8 (b)) are shown in figure 3 12 For the purposes of ray-tracing, source displacement was achieved by rotating the source about the mirror pole in increments of 0 127° The average ratio of source displacement to image displacement was 1 55, a comparable figure to the calculated magnification of 1 64

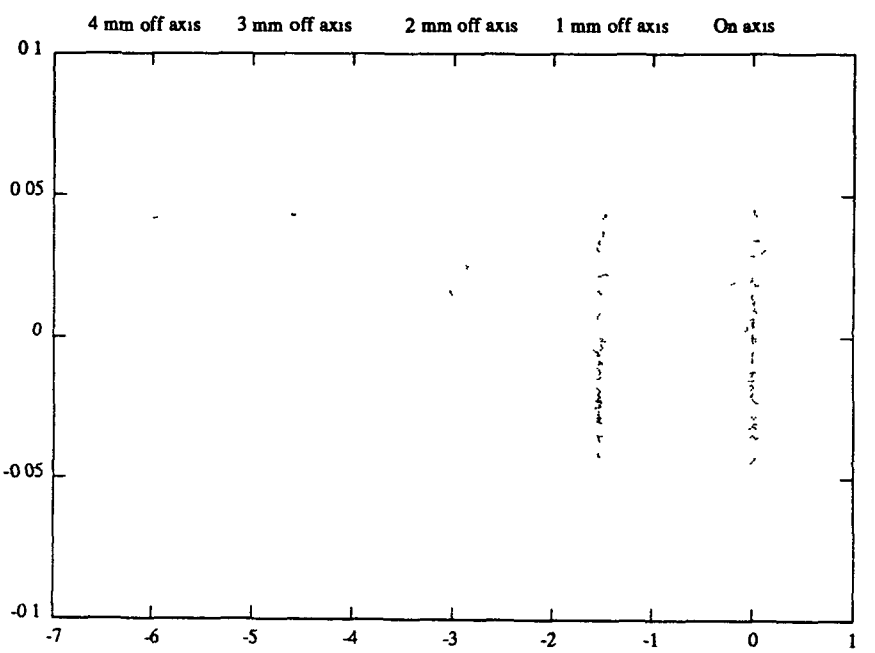

Figure 3.12. Monochromatic images (16 8 nm) produced by various point source positions.

The image widths (y direction) were measured to be approximately 0.1 mm as before, with only the slightest broadening ocurring at the larger displacements, indicating that the grating focusing remained relatively unimpaired.

The image lengths (measured in the x direction, as usual) were seen to increase as blurring was introduced by displacing the source. This is coupled with an increased loss of admitted flux as the the source was moved from its correct position. The on-axis image features about 300 points, this falls to about 90 points 4 mm off axis. The theory is again in general agreement with the observations, as the focusing conditions of the mirror can only be fulfilled for one point source position, with a gradual decay in focusing as the source point is moved.

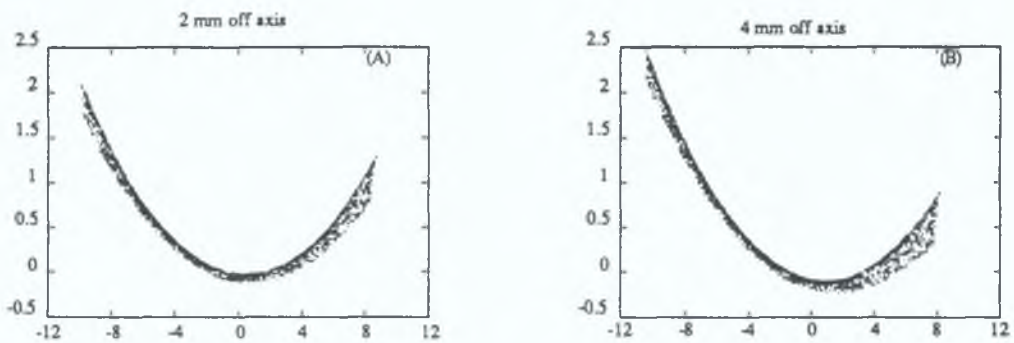

Figure 3.13. The effect of source displacement on primary image (see also figure 3.9, P 53).

To find the cause of these effects, the primary image was first examined, as this determined how the radiation was coupled into the spectrograph. What was observed, as summarised by figure 3.13 (a) and (b), was that as the source was moved off the axis, the primary image was skewed sideways in a direction opposite to the source displacement (compare figures 3.13 and 3.9). The effect of this was that the intersection of image and slit gradually changed from one central region to two separate regions separated by some 4 mm.

By inspection of the grating footprint (figure 3.14, which is similar to figure 3.10 except not blurred by the spatial extent of the source), the effect of this can be clearly seen. As the source was moved, the footprint shifted (in a direction opposite to the source displacement) and gradually split until two distinct portions of the grating were being utilised.

The effect on an astigmatic image (produced at 11.8 nm) of two resolved sources using two parts of the grating can be seen in figure 3.15. The off-axis image was split into two on the Rowland circle (this was not observed in figure 3.12 as the stigmatic conditions focus all the light from the grating into a single image) by an amount proportional to its distance from the optimum wavelength. In the case of the real system, the overlap between image and slit was adjustable by fine-tuning the mirror position. Thus by centring the slit in the width of the image, the onset of effects caused by double illumination of the slit could by prevented until the source displacement was close to 4 mm. As such large displacements were not generally required (see section 4.1.1), such image "forking" did not cause problems, once the

experimental technique had been perfected.

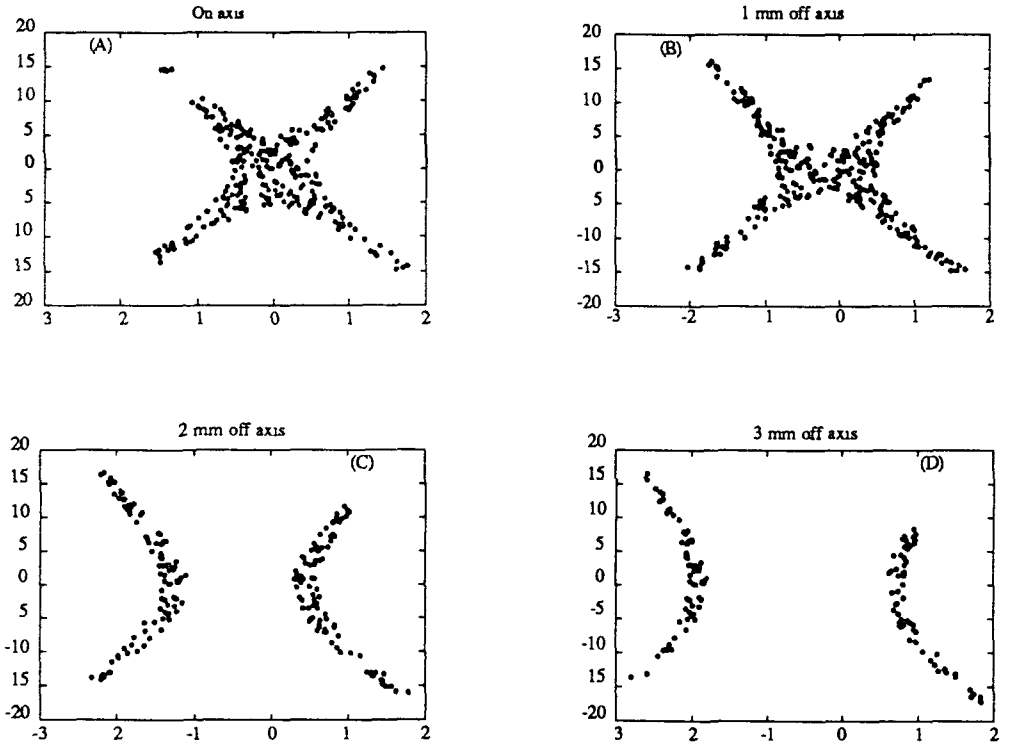

Figure 3.14. The effect of source displacement on grating footprint.

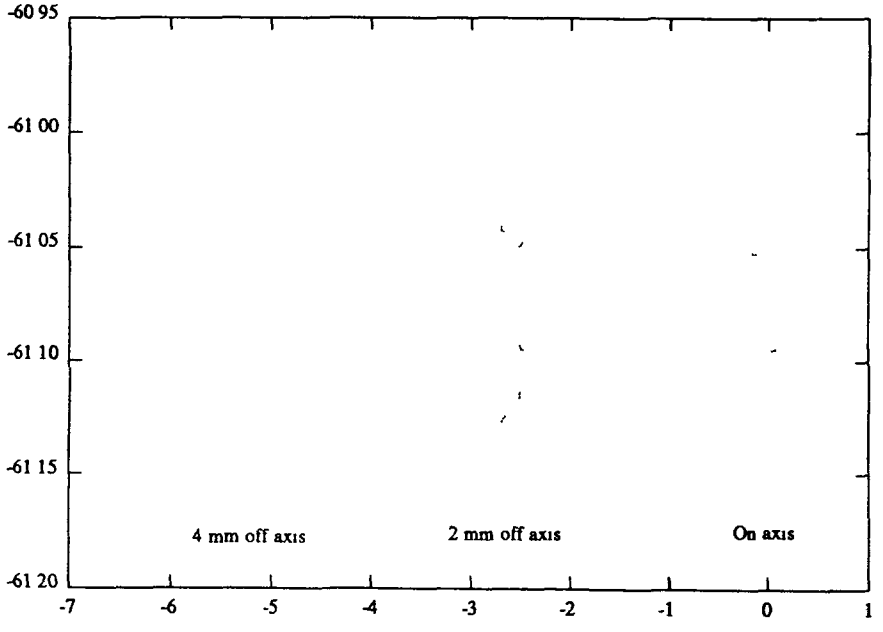

Figure 3.15. The effect of source displacement on image at 11 8 nm

3.5 4 Concluding remarks

Thus the process by which the modifications required to introduce the toroidal mirror into the spectrograph has been described, from design to commissioning the system and running experiments Ray-tracing methods were applied to analyse the optical characteristics All that remains is to present the experimental results obtained and to conclude the thesis with a discussion of the capabilities of the system as a research instrument

References

1 Galliou, P , M Sc Thesis, Universite P et M Curie (Paris, France) (1986) (unpublished work)

2 Barbee, T W , Opt Eng , 25, 898 (1986)

3 Henke, B L , At Dat & Nuc Tab , 27, 1 - 144 (1982)

4 Cromer, C L , Bridges, J M , Roberts, J R and Lucatorto, T B , Appl Opt , 24, 2996 (1985)

5 Chambers, A , Fitch, R K , Halliday, B S., *"Basic Vacuum Technology"*, Adam Hilger (1989)

6 Costello, J T , private communication

Chapter 4

Results, comparisons and conclusions

This chapter contains a presentation of the experimental results obtained using the stigmatic spectrograph which was commissioned in the course of the research described in this thesis The spectra produced are compared to the results of the ray-tracing described in detail in chapter 3. The discussion includes a system appraisal based on determination of the gains achieved by incorporating the toroidal mirror into the system and a description of the spatial properties of the imaging system with respect to the production of absorption spectra

4.1 Experimental results

The experimental procedure to produce a single absorption spectrum is described in section 3 4 To utilise the spatial properties of the imaging system (and to test the validity of the modelling techniques discussed in section 3.5), several spectra were recorded on one plate by repeatedly exposing the plate with the probe plasma moved off the axis (in the *wl* plane) by equal increments between each exposure (see figure 3.12). The probe displacement being directed away from the absorbing target surface and all other experimental conditions being held constant, the net effect was to produce a set of absorption spectra taken under identical conditions (within the limits of experimental error) except that the probe beam passed through a different region of the absorbing plasma during each exposure Several such multi-spectrum experiments were performed using different inter-plasma time delays (denoted by Δt) The spectra produced are shown in figure 4 1 Spectra (a), (b), (c) and (d) are details of plates, photographically enlarged by a factor of 3 for clarity Spectrum (e) is an actual size (contact) print of (d) The emission features superimposed on the absorption spectra were produced by the absorbing plasma

4.1.1 Comparison of ray-tracing to experimental results

As observations from plates were used to compile an applicable source model (see section 3 5 1), the measured width of the continuum bands (in figure 4.1) will obviously agree with ray-tracing. No other experimental data were used in the modelling process

Figure 3.11 and the relevant text describe the expected characteristic features of the continua. (e) shows a contact print of a multi-spectrum plate which spans a spectral range of about 5 to 16 nm. Concentrating on the form of the continua, it is clear that they appear very much as predicted. The change in the width of the bands as a function of wavelength (as explained in terms of linear magnification) is one of the most striking features of the spectrum. Also striking is the observed degradation of continuum profile as the wavelength deviates from the central region, detected by the change in continuum edge definition along the plate. This indicated that the monochromatic image of the source was focused at some point in the spectrum with the image going out of vertical focus with changing wavelength.

It is interesting to note that the stigmatic wavelength did not occur where predicted. The most sharply focused image appeared to be at about 9 nm, not at 16.8 nm. A simple calculation (see equations (1.12), (1.27), (1.28) and (1.29)) showed that the effective source condition required to produce a stigmatic image at 9 nm (*i.e.* r_v = -337 mm) was that the angle of incidence on the mirror be equal to 85.728° (a shift of just over ¼ of a degree). This was equivalent to displacing the source by 2.1 mm from its correct position. This also had the effect of changing the primary image distance from 150 mm to approximately 164 mm, an undesirable side-effect which would result in loss of light (if the mirror-slit distance were not adjusted) as the image on the slit would be out of focus. Examination of earlier (emission) spectra, taken while testing the apparatus, showed that when the system was first aligned, the stigmatic wavelength was at about 15 nm. This gradually moved to 9 nm during the course of the experiments, fortunately without a noticeable loss of density on the plates.

Examination of off-axis imaging was carried out by inspecting the series of adjacent spectra for the types of degradation observed in figures 3.12 and 3.15.

The increase in spatial aberration and the accompanying loss of admitted flux that resulted from imaging off-axis source points (figure 3.12) are clearly observable in figure 4.1. The fall in plate density with distance from the optic axis is seen on (b) and (c). The outermost continuum on (b) almost disappears at 15 nm. On (e) it can be seen that the two outermost bands are only barely resolvable at 16 nm due to the effects of spatial aberration, whereas they can be clearly resolved at around 9 nm due to the increased (vertical) focusing.

The effect of off-axis imaging on an astigmatic image, when the effects of double illumination (see section 3.5.3, p 58) of the slit were not correctly compensated for, can be seen in the uppermost continuum of (e). This reference continuum was taken so that tantalum self-absorption features could not be confused with aluminium features. It was placed inside the region normally shadowed by the absorbing target, a region for which the system had not been optimised. The result was that the spectrum split into two separate continua at around 10 nm, the split widening along the plate as expected. Little can be deduced from the location or extent of this "forking" as, experimentally, the objective was to avoid it, not to analyse it, thus measures had been taken to displace it from its natural position.

Knowing the distance between source locations that produced adjacent continua (see

section 4 1 2, below), the magnification (at a particular wavelength) can be deduced from measurement of image locations At 16 nm this was found to be a factor of about 1 6, in agreement with both theory and ray-tracing

Thus it may be concluded that the relatively simple model, applied to the optical system using ray-tracing, was found to be quite accurate, predicting the salient features of the experimentally produced spectra In particular, its provision of both an explanation of and a solution to the problem of spectral forking was most useful in perfecting the experimental technique

4.1 2 Spatial characteristics of plasma scanning

The choice of probe plasma positions were made on the basis that adjacent spectra must be clearly resolved (in the region of the stigmatic wavelength) so that they could be analysed separately if necessary Thus for two adjacent images of a plasma of 0 25 mm diameter to be separated by, say, 0 15 mm, required a centre to centre spacing of 0 40 mm This was applied in all the spectra shown with the exception of (a), where 0 50 was used As expected, the spectra are clearly resolved in the spectral regions shown in (a) to (d)

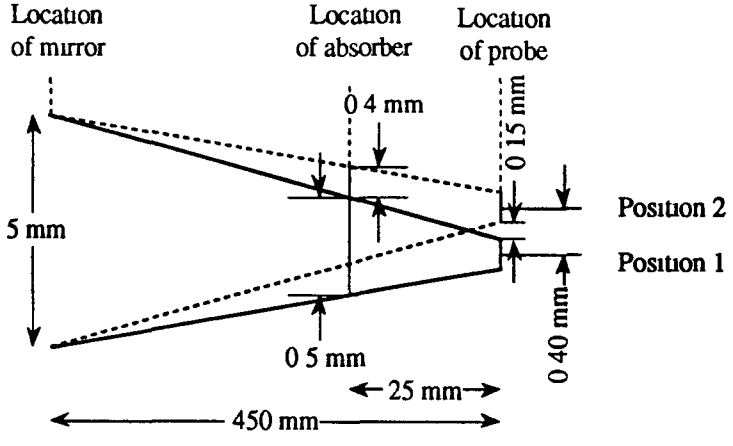

Figure 4 2. The geometry of source displacement (not to scale)

To determine the spatial resolution of this scanning technique at the absorbing plasma, the geometry of the front end optics was examined (see figure 4 2) Taking the effective width of the mirror to be 5 mm (see section 3 5 3) and the inter-plasma separation to be 25 mm, geometrical analysis showed that the beam had a width of approximately 0 5 mm at the absorber and was displaced by almost 0 4 mm by a source displacement of 0 4 mm Thus two adjacent continua probed a combined width of 0.9 mm, *i e* there was an overlap of the region probed by adjacent spectra of about 0.1 mm or 20 % Simply stated, the spatial resolution is about 0.5 mm at the absorber, *i e* only adjacent bands in (a) are fully resolved. In reality, an overlap of 20 % is small enough to resolve trends in the spatial behaviour of the absorber.

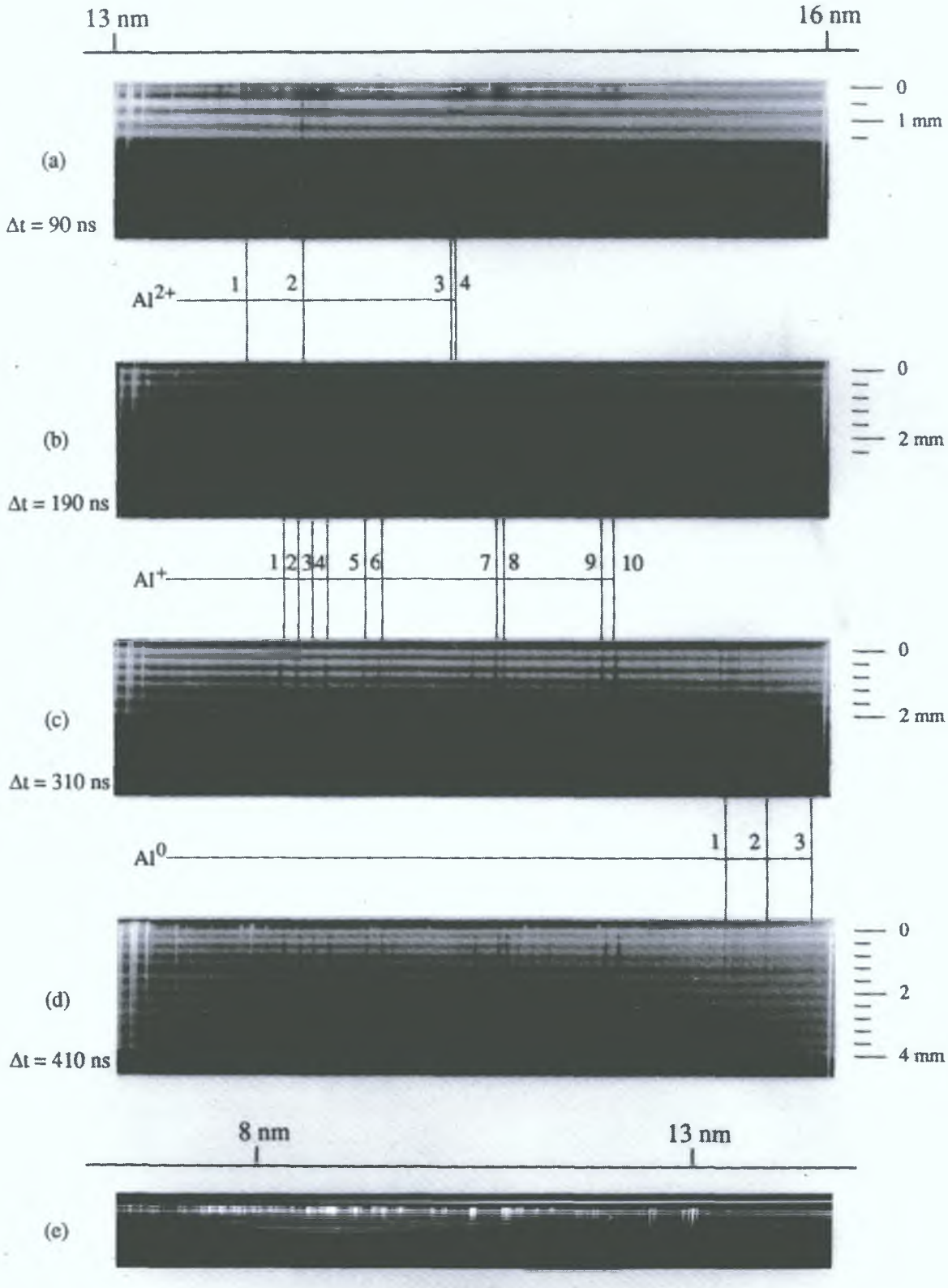

Figure 4.1. Aluminium photoabsorption spectra taken using the modified 2 m grazing incidence spectrograph (see table 4.1 for wavelengths of labelled features).

4.1.3 The application of plasma scanning

The modifications were made to the spectrograph so that stigmatic absorption spectroscopy of laser plasmas could be carried out in the XUV region. The spatial properties of the modified system were utilised in the development of the plasma scanning technique, these properties have been described in the previous sections. The application of this technique to absorption spectroscopy is now discussed.

The four enlarged spectra shown in figure 4.1, *i.e.* (a), (b), (c) and (d) respectively, show aluminium absorption spectra from 13 to 16 nm[15] taken using a range of inter-plasma time delays (as shown on figure 4.1). The length of plasma (above the target surface) scanned was increased with time delay, to account for the increased time over which expansion occurred.

The four spectra thus contain both spatial and temporal information about the evolution of the plasma. With the help of previous work [1, 2[16], 3], a selection of the absorption features associated with neutral, singly and doubly ionised aluminium (denoted Al^0, Al^+ and Al^{2+} respectively) have been identified (see table 4.1, see also figure 4.1). While a detailed analysis of these spectra is beyond the scope of this present work, a brief examination of them is sufficient to demonstrate the usefulness of the system.

	Al^0	Al^+	Al^{2+}
1	15.545	13.696	13.556
2	15.727	13.761	13.783
3	15.925	13.816	14.395
4		13.879	14.417
5		14.038	
6		14.099	
7		14.589	
8		14.623	
9		15.091	
10		15.036	

Table 4.1. Transition wavelengths (in nm) for features labelled on figure 4.1.

The advantages of time-resolved studies, as previously described[17], are clearly illustrated by (a) to (d).

Spectrum (a), probed 90 ns after generating the absorbing plasma (Δt = 90 ns), contains several strong Al^{2+} features, line 2 (Al^{2+}) being particularly intense. Several Al^+ features can also be seen, most of them being of lower intensity than the Al^{2+} features, with the exception of the lines, 7, 8, 9 and 10 (Al^+). These lines appear to be saturated, the strong

[15] The emission lines used as references actually occur at 13.041 and 16.007 nm respectively.

[16] One of the plates produced (specifically the Al^+ features of spectrum (c)) in the course of the research described in this thesis was being analysed for publication at the time of writing.

[17] See reference [7], chapter 1.

absorption broadening the observed linewidth. These observations show that at this stage the plasma was highly ionised, containing high densities of Al^{+} and Al^{2+} ions. Higher ion species may also have been present, but not in sufficient densities to observe their absorption spectra.

By inspection of spectrum (b) (Δt = 190 ns), the appearance of new Al^{+} structures (lines 1 and 2) and a loss in intensity of Al^{2+} features (lines 3 and 4 are barely discernible) can be observed. Overall, the Al^{+} features became more dominant at 190 ns. This indicates a drop in plasma temperature with time. It can also be seen that lines 7, 8, 9 and 10 (Al^{+}) appear narrower in (b) than in (a), indicating that they are no longer saturated. Thus either the absorption length or ion density (or both) had fallen with time, allowing some transmission where absorption had previously occurred.

In spectrum (c) (Δt = 310 ns), the Al^{2+} features have disappeared, leaving a clear, intense set of Al^{+} structures. A large number of new lines has appeared on the right-hand side of the spectrum. These lines, attributable to Al^{0}, are of considerably lower intensity than the Al^{+} features. The appearance of Al^{0} features indicates that a further drop in temperature had occurred accompanied by sufficient electron-ion recombination to produce an absorbing density of aluminium atoms.

Spectrum (d) (Δt = 410 ns) is similar to (c) in that it contains only Al^{0} and Al^{+} features. The Al^{+} lines are of lower intensity than those of (c), with some of the weaker structures having almost disappeared. Conversely, the Al^{0} features appear more intense, as is clearly demonstrated by comparing line 3 (Al^{0}) in (c) to that in (d). Many of the weaker Al^{0} structures observed in (d) are hardly seen at all in (c). This indicates further recombination had occurred, increasing the density of aluminium atoms.

Having identified a sample of spectral features and examined the spectra in terms of the temporal evolution of the plasma, a further examination of the spectra to demonstrate the advantages of producing spatially resolved images is presented. The scale on the right-hand side of each spectrum indicates the displacement (in millimetres) of the continuum source from its initial position. This gives the altitude above the target surface that was probed.

On examination of the Al^{+} features in (a), it can be seen that they are all of approximately the same length (within the resolution limits described in section 4.1.2). This is quite pronounced in lines 5 - 10 (Al^{+}), which are clearly observed with differing relative intensities in the first two continua (at 0 and 0.5 mm displacement respectively) and are not present at 1.0 mm displacement or above. In fact, this phenomenon was observed in all such spectra and is particularly clear in (c) and (d) where the Al^{0} structures are only observed up to an altitude of 1.2 mm.

This observation has two consequences. Firstly, it facilitates the study of the evolution of the plasma in terms of the generation and spatial distribution of different ion stages and secondly, the consistency of the observations allows unidentified lines to be attributed to a particular ion species by their spatial profile.

Returning to the Al^+ features of (a), an obvious change in the linewidths of 7 - 10 (Al^+) can be observed over the two continua. Thus indicating that the factors producing saturation (mentioned above) could be studied spatially as well as temporally. Similarly, the changes in the relative intensity of the lines that are observed in all such spatially resolved spectra contain a wealth of information about plasma evolution and dynamics.

Particularly striking, for example, is the consistent observation that the lower ion stage features of a spectrum were only observed in the region close to the target surface, while absorption by the higher ion stage was observed over a broader spatial region. In (d), for example, Al^0 features are only observed within 2 mm of the target surface whereas absorption by Al^+ ions is observed at up to 4 mm. Similarly line 2 (Al^{2+}) of (b) appears to gain strength with altitude, while the Al^+ lines behave in exactly the opposite manner. This can be explained in terms of the fact that a stream of ions continuously emanates from the plasma during its lifetime. This stream primarily consists of one dominant ion species. In an aluminium plasma at 310 ns (see spectrum (c)), Al^+ was the dominant species, the line intensity indicating that its density peaked at about 1 mm above the target surface and was sufficient to be observed up to at least 2 mm from the surface. The rapid fall in line intensity close to the surface indicates that the ions within the plasma had nearly all recombined to produce aluminium atoms. As this recombination had been producing neutrals for up to about 100 ns, the atoms had had time to stream out about 1.2 mm from the target.

4.1.4 Concluding remarks

The above examination indicates the broad range of phenomena which could be studied with the instrument in question. Restricting the remarks to the area of photoabsorption spectroscopy, for which the instrument was actually designed, it can be concluded from the preceding discussion that the plasma scanning technique can be used to attempt to produce pure absorption spectra of selected ion species by probing a selected portion of the absorber. The success of such experiments (*i.e.* the purity of the resultant spectra) would depend on the choice of element and skill of the experimenter.

4.2 Before and after : an optical comparison

In the literature [4], estimations of the gain in intensity in comparable optical systems were made by taking the product of the gain in geometrical focusing, the gain in system aperture and the mirror reflectivity. Thus the gain was expressed in terms of the increased image brightness achieved by compensating for astigmatism and the increased amount of light coupled into the system by adding a light collector (mirror). This was based on the assumption that *all other things being equal*, the above geometrical considerations (adjusted for losses at the mirror) account for the optical gains. This clearly does not apply to the two systems in

question as the insertion of the mirror required that the source be displaced by a considerable amount This in turn implied that the increase in aperture could not be directly related to the increase in admitted flux The alternative was to make a comparative ray-tracing study of the toroidal and non-toroidal systems by applying a standard source model to both and comparing the losses at their respective optical elements

The optical gain achieved by incorporating the toroidal mirror into the system is now discussed using the results of the ray-tracing analyses presented in sections 2 5 and 3 5 The gain was calculated at the optimum by using a monochromatic source emitting at 16 8 nm

4.2.1 Gain in admitted flux

To estimate the gain in admitted flux achieved by modifying the optics of the system, a standard source (Source 1, see section 3 5 1) was applied to both the optical systems The number of rays transmitted were then compared

5 4 % of the source passed through the slit of the non-toroidal system 65 % of this was incident on the grating's ruled area Thus 3 5 % of Source 1 was incident on the grating

Approximately 20 % of the standard source was incident on the toroidal mirror 5 0 % of the rays incident on the mirror were focused through the slit and onto the grating, ignoring reflection losses This figure fell to 4 4 % when losses at the mirror were included (mirror reflectivity, R, for 16 8 nm radiation incident at an angle of incidence of 86° was calculated to be $R = 0\ 87$) Thus 0 8 % of the rays from Source 1 were focused onto the grating

Ignoring losses at the grating, as they will be the same for both systems, the ratio of admitted fluxes shows that the non-toroidal system admitted 4.2 times more light than the toroidally focused system, *i e* introduction of the toroidal optics produced a loss in admitted flux by a factor of 0 24. This was due to the displacement of the source from 60 mm from the slit to 450 mm from the mirror

4.2.2 Focusing gain

This component of the gain is the effect of compensating for astigmatism to concentrate the light in shorter, more intense spectral lines

The length of the astigmatic spectral line (non-toroidal system, see 2 5 3) at 16 8 nm was measured at 75 mm (from figure 2 5, the ray-traced astigmatic spectrum)

The length of the stigmatic spectral line (toroidal system, see 3 5.3) at 16 8 nm was found to be 0 5 mm (from figure 3.11 (b), the ray-traced stigmatic spectrum).

The optical gain produced by the introduction of stigmatic focusing was in the ratio of the line lengths, which was thus equal to a factor of 150.

4.2.3 Overall intensity gain

An estimate of the intensity gain factor, g, was calculated to be the product of gain components described above This can be evaluated as

g = (gain in admitted flux) x (focusing gain)
= 0 24 x 150
= 36 at 16 8 nm

As this was calculated for the optimum wavelength, it is obviously the optimum gain The dependence of g on wavelength was due to the variation of mirror reflectivity and the respective line lengths on the Rowland circle. For example, g had a calculated value of approximately 30 at 12 nm and 25 at 20 nm

The gain can be termed the *increase in speed* of the instrument achieved by the incorporation of toroidal optics as it represents the increase in the amount of light received by the detector at the location of the monochromatic image at a certain wavelength It is thus related to the increase in plate density by the response of the photographic emulsion As the facilities for measurements of plate densities were not available at the time of writing, the experimental gain was not properly determined A rough estimate can be deduced from the fact that since the system has been modified, the number of laser shots required to produce a spectrum has been reduced by a factor of around 20 Discrepancies between this and the calculated value being attributable to imperfections in the models applied and the non-linear response of the emulsion

4.3 A critical appraisal

In this section, the results of the modifications made to the spectrograph are discussed in a practical framework of its application to the study of the photoabsorption spectroscopy of laser plasmas

4.3 1 Theory

From a theoretical point of view, the addition of a toroidal mirror to compensate for the main imperfections of the concave grating was an elegantly simple solution to the problem It not only allowed the removal of astigmatism without causing degradation of the image at the Rowland circle, but facilitated the simultaneous compensation of the three major problems posed by using a grazing incidence instrument to produce spectra from small sources.

4.3.2 Implementation

The accuracy of the implementation of the solution obviously depended on the mechanical constraints involved. Not least of these is the manufacture of the mirror. However, as the toroidal mirror features two orthogonally arranged circular radii, toroidal surfaces of similar quality to spherical ones could be produced.

The nature of the optical system, the elements being separated by reasonable distances and the spectrograph being fully self-contained, facilitated the use of a modular housing design which featured many standard vacuum components. System components, like the target holders, pressure sensors etc., were generally mounted on vacuum flanges which were clamped or bolted onto ports or cube faces via O-ring seals. This enabled easy access to such components for cleaning, repair etc.. The use of 40 mm ports and piping kept the internal volume (and hence internal surface area) small. This, and the relatively large pumping speed supplied by the vacuum system, made for rapid evacuation.

The small deflections of the optic axis introduced by the small grazing angles at the mirror and grating made the system long and narrow. At almost 2 m, it was considered too long to be housed on a single mounting table. The format adopted was that of two heavy steel plates supported by box-section frames sitting on adjustable rubber pads, the spectrograph sat on one table with the chambers mounted on the other. The absence of a rigid mechanical link between the slit and the mirror was possibly the single greatest source of alignment drift. It was strongly suspected that the effect of this was exacerbated by a gradual warping of the steel plates under their own weight.

While the system design was generally versatile and effective, if a little prototypical, the financial constraints placed on the project restricted the attention paid to details, such as micropositioners etc., required to achieve a high degree of systematic accuracy.

4.3.3 Experiment

While the system suffered from alignment drift, due to a number of factors, which could not be accurately monitored by mechanical means, it could be both monitored and compensated for using the operational and experimental alignment techniques described previously (see sections 3.4.2 and 3.4.2 respectively). The keeping of written records was essential to the monitoring process.

The systematic difficulties encountered while running experiments would probably have been considered typical of any such instrument. Time- and space-resolved absorption was inherently tricky to achieve, especially when it had to be achieved repeatedly in order to record a clear spectrum, as failure to get absorption on one shot would record a continuum that could obliterate weak absorption features. The increase in speed of the toroidal system, and resultant reduction in the number of shots required, considerably reduced the risk of this.

The reduced number of shots and pumping time combined to make the experiment

much less time consuming Two full experiments or one experiment with four or five repeat exposures could be performed in one day There was little difficulty in recording the individual time delay values and monitoring target damage when only 10 shots per exposure were required With the careful application of the experimental guidelines described in 3 4, almost a 100 % success rate was achieved in recording clear, bright absorption spectra This, coupled with the increased amount of information recorded on each plate represented a considerable increase in the efficiency of plate usage

4.3.4 Extended stigmatism

From the analysis of stigmatic wavelength location (see 4 1 1) it may be concluded that the apparatus would be suitable for the stigmatic spectroscopy of small sources over an extended spectral range by simply introducing small variations in the angle of incidence on the toroidal mirror Varying the angle between 85 728° and 86 183° facilitates placing the stigmatic wavelength anywhere between 9 and 25 nm without any appreciable loss in image intensity or having to reposition any of the optical elements A configuration to perform this function over a wavelength interval of 1 - 30 nm by varying the distances between the optical elements was previously proposed by G Tondello[18] While Tondello's method offers a wider spectral range, the practical difficulty in varying the position of source and mirror (relative to the spectrograph) would be considerable, not to mention requiring expensive modifications

The system could be modified for high-resolution spatial studies by simply aperturing the probe This would, of course, greatly reduce the speed, requiring many more laser shots to produce a spectrum As increased speed was one of the objectives of this project, this was not really considered as part of the work described within these pages

4.3.5 Concluding remarks

To correct the main design fault discussed in 4 3 1 would not require major expenditure The most cost effective and stable mounting structure would probably be a cast concrete plinth supported on columns to replace the two tables The only other major improvement would be to redesign the mirror and target mounts for more precise control While this would take some of the art out of the experimental process, the cost of precision stages could make it prohibitively expensive

From the preceding presentation of results and discussions, it is concluded that the system was capable of performing the function for which it was designed, *i e* the production of absorption spectra of selected ion species by probing a suitable region of the absorbing plasma with a continuum beam Furthermore, the production of such spectra required only familiarity with the equipment gained through experience, no special knowledge of toroidal optics was necessary

[18] See reference [9], chapter 1

References

1 Brilly, J , Kennedy, E T and Mosnier, J - P , J Phys B , 21, 3685 (1988)

2 Costello, J T, Evans, D , Hopkins, R B , Kennedy, E T, Kiernan, L , Mansfield, M W D , Mosnier, J - P, Sayyad, M H and Sonntag, B F (to be published)

3 Cantu, A M and Tozzi, G P, J Opt Soc Am , 72, 729 (1982)

4 Cantu, A M and Tondello, G , Appl Opt , 14, 996 (1975)

Acknowledgements

First and foremost I would like to thank Jean-Paul Mosnier for his guidance, encouragement, words of wisdom and the occasional pint of Guinness I would also like to thank John Costello for his technical assistance and Eugene Kennedy for advice, enthusiasm and generally keeping it all together

I am grateful to Mike Mansfield and the U.C C. workshop for manufacturing the main components of the cube system and to Des Lavelle and Cian Merne of the school workshop for design consultations as well as manufacturing many of the ancillary components Thanks to Berndt Sonntag and his researchers at DESY for their assistance with the ray-tracing and their hospitality and also to Al Devine for preparing the print of figure 4 1

I would like to acknowledge the financial help received from Louth Co Council during my years as an undergraduate This proved to be invaluable in relieving the financial pressure placed on both my parents and myself by the high cost of education.

I would also like to thank my family and friends, particularly those to whom this thesis is dedicated Their encouragement was invaluable I am especially indebted to Karen, whose continuing support is very much appreciated